J. Fluid Mech. (2001), *vol.* 440, *pp.* 75–116. Printed in the United Kingdom

Large-eddy simulation of free-surface turbulence

By LIAN SHEN AND DICK K. P. YUE

Department of Ocean Engineering, Massachusetts Institute of Technology, Cambridge, MA 02139, USA

(Received 3 April 2000 and in revised form 9 November 2000)

In this paper we investigate the large-eddy simulation (LES) of the interaction between a turbulent shear flow and a free surface at low Froude numbers. The benchmark flow field is first solved by using direct numerical simulations (DNS) of the Navier–Stokes equations at fine ($128^2 \times 192$ grid) resolution, while the LES is performed at coarse resolution. Analysis of the ensemble of 25 DNS datasets shows that the amount of energy transferred from the grid scales to the subgrid scales (SGS) reduces significantly as the free surface is approached. This is a result of energy backscatter associated with the fluid vertical motions. Conditional averaging reveals that the energy backscatter occurs at the splat regions of coherent hairpin vortex structures as they connect to the free surface. The free-surface region is highly anisotropic at all length scales while the energy backscatter is carried out by the horizontal components of the SGS stress only. The physical insights obtained here are essential to the efficacious SGS modelling of LES for free-surface turbulence. In the LES, the SGS contribution to the Dirichlet pressure free-surface boundary condition is modelled with a dynamic form of the Yoshizawa (1986) expression, while the SGS flux that appears in the kinematic boundary condition is modelled by a dynamic scale-similarity model. For the SGS stress, we first examine the existing dynamic Smagorinsky model (DSM), which is found to capture the free-surface turbulence structure only roughly. Based on the special physics of free-surface turbulence, we propose two new SGS models: a dynamic free-surface function model (DFFM) and a dynamic anisotropic selective model (DASM). The DFFM correctly represents the reduction of the Smagorinsky coefficient near the surface and is found to capture the surface layer more accurately. The DASM takes into account both the anisotropy nature of free-surface turbulence and the dependence of energy backscatter on specific coherent vorticity mechanisms, and is found to produce substantially better surface signature statistics. Finally, we show that the combination of the new DFFM and DASM with a dynamic scale-similarity model further improves the results.

1. Introduction

The interaction of turbulence with a free surface is a problem of fundamental interest and important to many applications. For instance, free-surface turbulent flows affect the rate at which heat and mass are transferred across the ocean surface, which has immediate as well as long-term environmental effects. Recent radar observations of ship wakes have also added new interest in the interaction of wake turbulence with surface waves. Free-surface turbulence is also of interest in a variety of industrial applications.

Free-surface turbulence has been studied by a number of investigators using direct numerical simulations (DNS) of the governing equations: to name a few, Lam

& Banerjee (1988), Handler *et al.* (1993), Komori *et al.* (1993), Borue, Orszag & Staroselsky (1995) and Pan & Banerjee (1995) for open-channel flows; Perot & Moin (1995) and Walker, Leighton & Garza-Rios (1996) for initially isotropic free-surface flows; Lombardi, De Angelis & Banerjee (1996) and Cortesi *et al.* (1999) for air–water mixing flows; and Shen *et al.* (1999) and Shen, Triantafyllou & Yue (2000) for the interaction between a turbulent shear flow and a free surface. Such DNS results provide detailed information on the statistical, structural and dynamical properties of free-surface turbulence and have led to appreciable steps towards its understanding.

While DNS resolves the essential turbulence scales and thus has the virtue that no *ad hoc* model is needed, it is limited to low Reynolds numbers and simple flow configurations. For most problems of importance to applications, the Reynolds numbers are high, DNS is incapable of covering the full (integral to dissipative) scale range, and turbulence modelling is essential. A promising approach in this case is the method of large-eddy simulation (LES), in which only the large (grid-scale, GS) motions are resolved explicitly, while contributions from subgrid-scale (SGS) motions are modelled. Since the introduction of LES in meteorology (Smagorinsky 1963), LES has been applied with some success to a variety of turbulence problems. Reviews on the development and application of LES can be found in Rogallo & Moin (1984), Lesieur & Métais (1996) and Meneveau & Katz (2000).

The development of LES for free-surface turbulence has been limited until recently. Dommermuth & Novikov (1993) used DNS and LES to study the interaction between turbulence and a free surface with and without surface waves. They employed a number of local and global SGS models and their combinations, but with limited success in that, as resolution is decreased, the closure models they considered work as poorly as grid filters with no SGS models. They concluded that it would be important to obtain a better understanding of the structure of the turbulence in question. Salvetti & Banerjee (1995) and Salvetti *et al.* (1997) developed a dynamic two-parameter model, which is a combination of the Smagorinsky model and the scale-similarity model (Bardina, Ferziger & Reynolds 1983) with both coefficients determined dynamically through the Germano identity (Germano *et al.* 1991). Their tests with decaying turbulence beneath a flat free-slip wall show that the dynamic two-parameter model obtains significant improvements over existing SGS models. Recently, Hodges & Street (1999) performed LES for a turbulent open-channel flow with a finite-amplitude surface wave. They employed the dynamic two-parameter model as the SGS model and obtained results for the turbulence–wave interactions.

Very recently, Dimas & Fialkowski (2000) proposed a novel large-wave simulation approach for the formulation of LES of free-surface flows at high Froude numbers. In this approach, the irregular mesh associated with the free-surface wave motion is transformed to a rectangular computational domain. By filtering the Navier–Stokes equations in the computational space, a new SGS term representing the small-scale surface-wave effects emerges, in addition to the usual SGS stress. As a first step in testing this new approach, Dimas & Fialkowski (2000) employed eddy-viscosity models with constant model coefficients for two-dimensional weak spilling breakers and obtained promising results.

The objective of the present study is to further develop large-eddy simulation capabilities for free-surface turbulent flows. As a canonical problem, we consider the interaction of a turbulent shear flow with a free surface at low Froude numbers. From previous DNS studies (cf. Shen *et al.* 1999, 2000), it is known that free-surface turbulent shear flow possesses a number of unique features: (i) The flow field near the surface is highly anisotropic. The vanishing of the tangential stresses at the surface

creates a thin *surface layer* where the velocity derivatives (e.g. vorticity and strain rate components) are highly anisotropic. On the other hand, the blockage effects of the surface cause anisotropy of the velocity components themselves over a much thicker region. (ii) This multi-layer structure is manifested in the turbulent diffusion, which can be interpreted analytically through a similarity solution for the mean flow (Shen *et al.* 2000). (iii) The free-surface turbulent flow is characterized by connection of coherent hairpin vortex structures at the free surface. Depending on the stage of the connection process, different vortex dynamics can be identified, which ultimately result in persistent surface-connecting vortices.

From the above, it is clear that the effectiveness of LES of free-surface turbulence would be enhanced if the characteristic features of the flow are taken into account and are captured by the SGS model(s) employed. In addition to the descriptions of the statistical and structural properties, of special importance in the context of LES is an understanding of the interaction and energy transfer mechanisms between resolved grid scales and the modelled subgrid scales of the flow. In this paper we investigate these inter-scale turbulent mechanisms near the free surface and use this understanding to develop specific SGS models which capture these underlying structures and mechanisms. The efficacy of these models is supported by extensive *a priori* and *a posteriori* LES tests.

This paper is organized as follows. We outline in § 2 the mathematical formulation and numerical method for the DNS and LES. In § 3, we analyse the DNS data to obtain the physical understanding necessary for the effective SGS modelling of free-surface turbulence. We investigate the energy cascade in the free-surface turbulence and use a conditional averaging technique to study the role of coherent vortex structures in the inter-scale energy transfer. We also examine the anisotropy of the flow field and the consequent implications for SGS modelling. The LES results are presented in § 4. We first investigate the modelling of the subgrid-scale contributions appearing in the boundary conditions. We then propose two new models for the SGS stress, a dynamic free-surface function model (DFFM) and a dynamic anisotropic selective model (DASM). These new models are evaluated in detail and are shown to be superior to existing models. Finally, we combine the new DFFM and DASM with a dynamic scale-similarity model to further improve the performance. In § 5 we present our conclusions.

2. Mathematical formulation and numerical method

2.1. *Governing equations*

We consider a turbulent shear flow beneath a free surface. As shown in figure 1, the coordinate axes x, y, z (also denoted as x_i, $i = 1, 2, 3$) respectively point in the mean flow streamwise, mean flow spanwise, and vertical upward directions. The origin is located at the undisturbed free surface.

The governing equations for the velocity components u_i (also denoted as u, v, or w) are the Navier–Stokes equations and the continuity equation:

$$\frac{\partial u_i}{\partial t} + \frac{\partial (u_i u_j)}{\partial x_j} = -\frac{\partial p}{\partial x_i} + \frac{1}{Re}\frac{\partial^2 u_i}{\partial x_j \partial x_j}, \quad i = 1, 2, 3, \tag{2.1}$$

$$\frac{\partial u_i}{\partial x_i} = 0. \tag{2.2}$$

Here and hereafter, all variables are normalized by the vertical extent L_0 and velocity

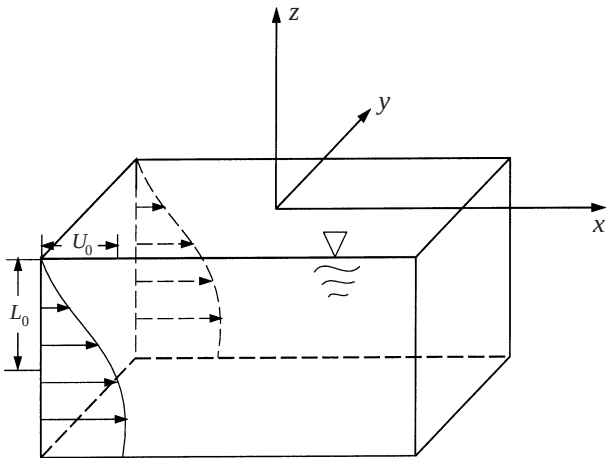

FIGURE 1. Schematic of a turbulent shear flow under a free surface.

deficit U_0 of the initial mean shear. The dynamic pressure p is normalized by ρU_0^2, where ρ is the fluid density. The Reynolds number is defined as $Re \equiv U_0 L_0/\nu$, with ν the kinematic viscosity.

In this study, for any variable $f(\boldsymbol{x})$, its grid-scale portion $\overline{f}(\boldsymbol{x})$ is obtained by using a low-pass filter $\overline{G}(\boldsymbol{x})$ (cf. e.g. Leonard 1974):

$$\bar{f}(\boldsymbol{x}) \equiv \int \overline{G}(\boldsymbol{x}-\boldsymbol{x}')f(\boldsymbol{x}')\,\mathrm{d}\boldsymbol{x}'; \tag{2.3}$$

and the subgrid-scale portion $f'(\boldsymbol{x})$ is defined as

$$f'(\boldsymbol{x}) \equiv f(\boldsymbol{x}) - \bar{f}(\boldsymbol{x}). \tag{2.4}$$

After applying the filter to (2.1) and (2.2), we obtain the governing equations for the grid-scale velocities:

$$\frac{\partial \bar{u}_i}{\partial t} + \frac{\partial \bar{u}_i \bar{u}_j}{\partial x_j} = -\frac{\partial \bar{p}}{\partial x_i} + \frac{1}{Re}\frac{\partial^2 \bar{u}_i}{\partial x_j \partial x_j} - \frac{\partial \tau_{ij}}{\partial x_j}, \quad i = 1,2,3, \tag{2.5}$$

and

$$\frac{\partial \bar{u}_i}{\partial x_i} = 0. \tag{2.6}$$

Here τ_{ij} is the subgrid-scale (SGS) stress defined as

$$\tau_{ij} \equiv \overline{u_i u_j} - \bar{u}_i \bar{u}_j, \quad i,j = 1,2,3, \tag{2.7}$$

which represents the contributions from the subgrid scales and must be modelled in terms of resolved quantities. In flows where only kinematic boundary conditions are imposed, it is conventional to model only the trace-free portion, M_{ij}, of τ_{ij}:

$$M_{ij} \equiv \tau_{ij} - \tfrac{1}{3}\delta_{ij}\tau_{kk}. \tag{2.8}$$

The isotropic part of the SGS stress is then absorbed into the (dynamic) pressure. Thus the momentum equation (2.5) becomes

$$\frac{\partial \bar{u}_i}{\partial t} + \frac{\partial \bar{u}_i \bar{u}_j}{\partial x_j} = -\frac{\partial \bar{P}}{\partial x_i} + \frac{1}{Re}\frac{\partial^2 \bar{u}_i}{\partial x_j \partial x_j} - \frac{\partial M_{ij}}{\partial x_j}, \quad i = 1,2,3, \tag{2.9}$$

with the modified pressure

$$\bar{P} \equiv \bar{p} + \tfrac{1}{3}\tau_{kk}. \tag{2.10}$$

In the presence of a free surface, dynamic conditions on the *total* stress are imposed and the decomposition (2.8) and (2.10) results in an additional SGS scalar, $p_{SGS} \equiv \tau_{kk}/3$, which must be modelled separately. This is discussed in § 2.2 and the performance of this modelling is evaluated in § 4.2.

2.2. *Boundary conditions*

We treat the bottom $z = -D$ as a flat free-slip boundary, which has the boundary conditions

$$\frac{\partial u}{\partial z} = \frac{\partial v}{\partial z} = w = \frac{\partial p}{\partial z} = 0 \quad \text{on} \quad z = -D. \tag{2.11}$$

After passing the filter (2.3), the bottom boundary conditions for the grid-scale motions have a similar form:

$$\frac{\partial \bar{u}}{\partial z} = \frac{\partial \bar{v}}{\partial z} = \bar{w} = \frac{\partial \bar{P}}{\partial z} = 0 \quad \text{on} \quad z = -D. \tag{2.12}$$

The boundary conditions for the deformable free surface are much more complicated. Assuming that the Froude number $F_r \equiv U_0/(gL_0)^{1/2}$ (g is the gravity acceleration) is small, we linearize the free-surface boundary conditions at $z = 0$. Neglecting surface tension effects and assuming constant pressure on the air side, the balance of the two tangential and one normal stress components at the free surface yields respectively the three dynamic boundary conditions

$$\frac{1}{Re}\left(\frac{\partial u}{\partial z} + \frac{\partial w}{\partial x}\right) = 0 \quad \text{on} \quad z = 0, \tag{2.13}$$

$$\frac{1}{Re}\left(\frac{\partial v}{\partial z} + \frac{\partial w}{\partial y}\right) = 0 \quad \text{on} \quad z = 0, \tag{2.14}$$

and

$$p = \frac{h}{Fr^2} + \frac{2}{Re}\frac{\partial w}{\partial z} \quad \text{on} \quad z = 0, \tag{2.15}$$

where $h(x, y, t)$ is the free-surface elevation.

Upon filtering, the dynamic free-surface boundary conditions for the grid-scale motions are obtained as follows:

$$\frac{1}{Re}\left(\frac{\partial \bar{u}}{\partial z} + \frac{\partial \bar{w}}{\partial x}\right) = 0 \quad \text{on} \quad z = 0, \tag{2.16}$$

$$\frac{1}{Re}\left(\frac{\partial \bar{v}}{\partial z} + \frac{\partial \bar{w}}{\partial y}\right) = 0 \quad \text{on} \quad z = 0, \tag{2.17}$$

and

$$\bar{p} = \frac{\bar{h}}{Fr^2} + \frac{2}{Re}\frac{\partial \bar{w}}{\partial z} \quad \text{on} \quad z = 0. \tag{2.18}$$

Because of the modification (2.10), the normal dynamic free-surface boundary condition becomes

$$\bar{P} = \frac{\bar{h}}{Fr^2} + \frac{2}{Re}\frac{\partial \bar{w}}{\partial z} + p_{SGS} \quad \text{on} \quad z = 0, \tag{2.19}$$

where the subgrid-scale contribution $p_{SGS} \equiv \tau_{kk}/3$ is unknown and needs to be

separately modelled. In this study, we model p_{SGS} by Yoshizawa (1986)'s expression:

$$\tfrac{1}{3}\tau_{kk} = 2C_p\bar{\Delta}^2|\bar{s}|^2. \tag{2.20}$$

Here $|\bar{s}| \equiv (2\bar{s}_{ij}\bar{s}_{ij})^{1/2}$ and $\bar{s}_{ij} \equiv (\partial\bar{u}_i/\partial x_j + \partial\bar{u}_j/\partial x_i)/2$. In a dynamic scheme, the coefficient C_p can be determined through the procedure developed by Moin *et al.* (1991) based on the Germano identity (Germano *et al.* 1991). To do this, we introduce a test filter $\widehat{G}$ in addition to the grid filter $\overline{G}$ and, let $\hat{\overline{G}} = \widehat{G}\overline{G}$. Applying $\hat{\overline{G}}$ to the Navier–Stokes equations, we obtain the subgrid-scale stress at the coarse filter level:

$$T_{ij} = \widehat{\overline{u_i u_j}} - \hat{\bar{u}}_i\hat{\bar{u}}_j, \quad i,j = 1,2,3. \tag{2.21}$$

The Germano identity gives the algebraic relation

$$\mathscr{L}_{ij} = \widehat{\bar{u}_i\bar{u}_j} - \hat{\bar{u}}_i\hat{\bar{u}}_j = T_{ij} - \widehat{\tau_{ij}}, \tag{2.22}$$

where $\mathscr{L}_{ij}$ is a function of $\bar{u}_i$ and is computable from the resolved variables.

Assuming that the same Yoshizawa expression can be applied to $T_{kk}/3$ with the same coefficient C_p:

$$\tfrac{1}{3}T_{kk} = 2C_p\hat{\bar{\Delta}}^2|\hat{\bar{s}}|^2, \tag{2.23}$$

we obtain

$$\tfrac{1}{3}\mathscr{L}_{kk} = 2C_p\hat{\bar{\Delta}}^2|\hat{\bar{s}}|^2 - 2C_p\hat{\bar{\Delta}}^2|\bar{s}|^2. \tag{2.24}$$

Simplification can be obtained if the coefficient C_p in (2.24) can be extracted from the filter operation in the last term. In general, this cannot be done directly (cf. Ghosal *et al.* 1995). For simplicity, we assume that C_p is constant on the horizontal plane and let the test filter $\widehat{G}$ operate in the horizontal directions only. Equation (2.24) then becomes

$$\tfrac{1}{3}\mathscr{L}_{kk} = C_p(2\hat{\bar{\Delta}}^2|\hat{\bar{s}}|^2 - 2\bar{\Delta}^2\widehat{|\bar{s}|^2}). \tag{2.25}$$

The coefficient C_p can be obtained by least-squares to best match the two sides of (2.25) on the free surface:

$$C_p = \frac{\langle m_I\mathscr{L}_{kk}/3\rangle}{\langle m_I^2\rangle} \quad \text{on} \quad z = 0, \tag{2.26}$$

where $m_I = 2\hat{\bar{\Delta}}^2|\hat{\bar{s}}|^2 - 2\bar{\Delta}^2\widehat{|\bar{s}|^2}$ and $\langle\,\rangle$ denotes the horizontal plane averaging.

The kinematic free-surface boundary condition, which states that the free surface is material, gives

$$\frac{\partial h}{\partial t} = w - u\frac{\partial h}{\partial x} - v\frac{\partial h}{\partial y} \quad \text{on} \quad z = h. \tag{2.27}$$

Upon Taylor expansion about $z = 0$ and using (2.2), we obtain

$$\frac{\partial h}{\partial t} = w - \frac{\partial}{\partial x}(uh) - \frac{\partial}{\partial y}(vh) \quad \text{on} \quad z = 0. \tag{2.28}$$

After filtering, the kinematic free-surface boundary condition becomes

$$\frac{\partial\bar{h}}{\partial t} = \bar{w} - \frac{\partial}{\partial x}(\bar{u}\bar{h}) - \frac{\partial}{\partial y}(\bar{v}\bar{h}) - \frac{\partial\tau_u^{kbc}}{\partial x} - \frac{\partial\tau_v^{kbc}}{\partial y} \quad \text{on} \quad z = 0. \tag{2.29}$$

Here

$$\tau_u^{kbc} \equiv \overline{uh} - \bar{u}\bar{h} \quad \text{and} \quad \tau_v^{kbc} \equiv \overline{vh} - \bar{v}\bar{h}, \tag{2.30}$$

which are additional unknown subgrid-scale quantities and must again be separately modelled. In this study we use scale-similarity models:

$$\tau_u^{kbc} \equiv \overline{uh} - \bar{u}\bar{h} = C_{kbc}(\overline{\bar{u}\bar{h}} - \bar{\bar{u}}\bar{\bar{h}}), \quad \tau_v^{kbc} \equiv \overline{vh} - \bar{v}\bar{h} = C_{kbc}(\overline{\bar{v}\bar{h}} - \bar{\bar{v}}\bar{\bar{h}}). \tag{2.31}$$

The coefficient, C_{kbc}, can again be determined dynamically as follows.

At the coarse filter level $\hat{\overline{G}}$, the SGS flux is written as

$$T_u^{kbc} \equiv \widehat{\overline{uh}} - \hat{\bar{u}}\hat{\bar{h}} = C_{kbc}(\widehat{\overline{\bar{u}\bar{h}}} - \hat{\bar{\bar{u}}}\hat{\bar{\bar{h}}}), \quad T_v^{kbc} \equiv \widehat{\overline{vh}} - \hat{\bar{v}}\hat{\bar{h}} = C_{kbc}(\widehat{\overline{\bar{v}\bar{h}}} - \hat{\bar{\bar{v}}}\hat{\bar{\bar{h}}}). \tag{2.32}$$

An algebraic identity similar to (2.22) gives

$$\left.\begin{aligned} \mathscr{L}_u^{kbc} &= \widehat{\bar{u}\bar{h}} - \hat{\bar{u}}\hat{\bar{h}} = T_u^{kbc} - \widehat{\tau_u^{kbc}} = C_{kbc}(\widehat{\bar{\bar{u}}\bar{\bar{h}}} - \hat{\bar{\bar{u}}}\hat{\bar{\bar{h}}}), \\ \mathscr{L}_v^{kbc} &= \widehat{\bar{v}\bar{h}} - \hat{\bar{v}}\hat{\bar{h}} = T_v^{kbc} - \widehat{\tau_v^{kbc}} = C_{kbc}(\widehat{\bar{\bar{v}}\bar{\bar{h}}} - \hat{\bar{\bar{v}}}\hat{\bar{\bar{h}}}). \end{aligned}\right\} \tag{2.33}$$

Here C_{kbc} is assumed to be constant on the free surface and is solved by least-square matching of (2.33) to give

$$C_{kbc} = \frac{\langle \mathscr{L}_u^{kbc} m_u + \mathscr{L}_v^{kbc} m_v \rangle}{\langle m_u^2 + m_v^2 \rangle} \quad \text{on} \quad z = 0, \tag{2.34}$$

where $m_u = \widehat{\bar{\bar{u}}\bar{\bar{h}}} - \hat{\bar{\bar{u}}}\hat{\bar{\bar{h}}}$ and $m_v = \widehat{\bar{\bar{v}}\bar{\bar{h}}} - \hat{\bar{\bar{v}}}\hat{\bar{\bar{h}}}$.

The performance of the SGS modelling for the free-surface dynamic and kinematic boundary conditions discussed here will be evaluated in § 4.2.

2.3. *Numerical method*

The numerical method for the DNS is given in detail in Shen *et al.* (1999). To summarize, the Navier–Stokes equations (2.1) together with the continuity equation (2.2) are solved as an initial-boundary-value problem. For the numerics, we use a periodic boundary condition in the horizontal directions and a vertically staggered grid system where u, v, p are assigned at regular grids while w is assigned at staggered grids. For space discretization, a sixth-order finite difference scheme is used in the horizontal directions and a second-order finite difference scheme is used in the vertical direction. A second-order Runge–Kutta scheme is used for time integration. The pressure at each Runge–Kutta time-substep is solved through a Poisson equation which is obtained by taking the divergence of the momentum equation and invoking the continuity equation.

The numerical scheme for the LES is essentially the same as that for DNS. The additional SGS stress terms are assigned at the vertically staggered grid system, with τ_{11}, τ_{12} (τ_{21}), τ_{22} and τ_{33} at regular grids, and τ_{13} (τ_{31}), τ_{23} (τ_{32}) at staggered grids. To calculate the derivatives of the SGS stress, we use a sixth-order finite difference scheme in the horizontal directions and a second-order finite difference scheme in the vertical direction.

For both DNS and LES simulations, the computational domain size is $L_x \times L_y = 10.472^2$ (horizontally) by $L_z = 6$ (vertically). The Reynolds number is $Re = 1400$ and the Froude number is $Fr = 0.7$. For DNS, we use a 128^2 (horizontal) $\times$ 192 (vertical) grid ($\Delta_x = \Delta_y \simeq 0.08$, $\Delta_z \simeq 0.03$) with timestep 0.005. The DNS grid discretizations are comparable to the Kolmogorov length scale, which for this Reynolds number and the turbulence energy dissipation rate from the simulations, is estimated to be $\eta \sim 0.03$. For LES we use a coarse 32^2(horizontal) $\times$ 96 (vertical) grid with timestep 0.02.

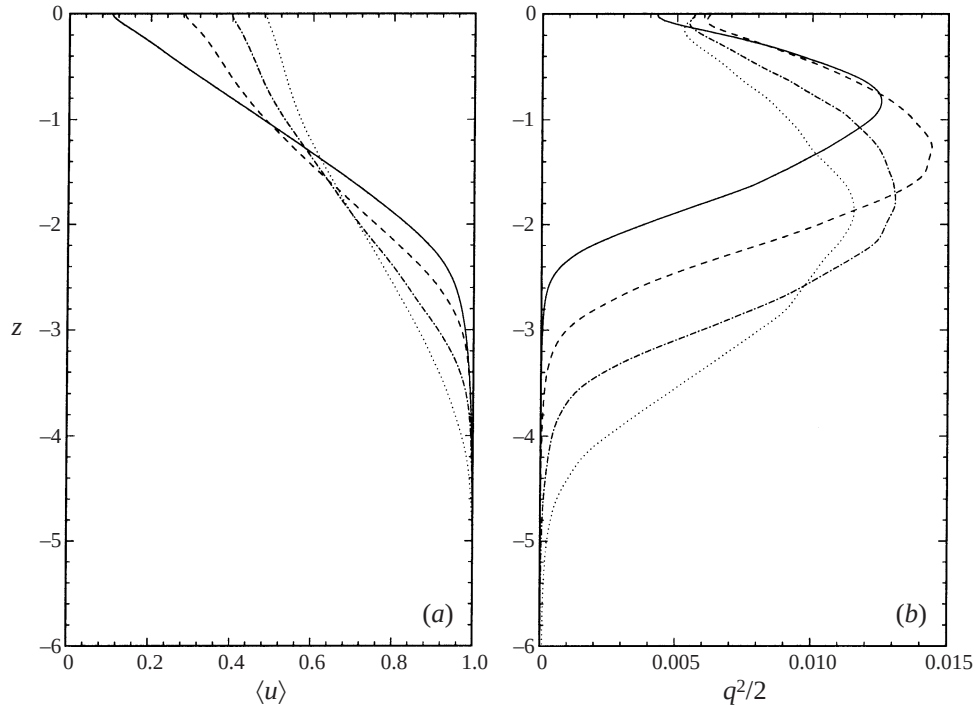

FIGURE 2. Time evolution of (*a*) the mean streamwise velocity $\langle u \rangle$, and (*b*) turbulent kinetic energy $q^2/2 \equiv \langle (u_i - \langle u_i \rangle)^2 \rangle / 2$, $i = 1, 2, 3$, as a function of depth: ———, $t = 20$; – – – –, $t = 40$; – · – · –, $t = 60$; · · · · · ·, $t = 80$.

3. DNS results for SGS modelling

3.1. *Overview of the flow field*

The direct numerical simulation starts with the initial mean velocity profile

$$u(z, t = 0) = 1 - 0.9988 \operatorname{sech}^2(0.88137\, z). \tag{3.1}$$

This profile corresponds to the mean velocity measured in the wake of a NACA 0003 hydrofoil (Mattingly & Criminale 1972). Small-amplitude divergence-free velocity noise is imposed upon this initial field, serving as the seed for turbulence. From this initial condition, DNS is performed to $t = 90$. To obtain converged statistics, we perform 25 repeated simulations with different initial seeds. All the statistical results we report in this paper are ensemble averaged over these simulations. In view of the horizontal homogeneity, spatial average over the horizontal (x, y)-plane is used unless otherwise pointed out.

Figure 2 shows the time evolutions of the mean streamwise velocity and the turbulence intensity depth profile. As expected, energy is extracted from the mean shear for turbulence production. Our interests are in the processes near the free surface. Figure 3 plots the evolutions of turbulent kinetic energy at the free surface and the fluctuation of surface elevation. For time between $40 \sim 75$, turbulence supply from the mean shear below is approximately balanced by dissipation (see § 3.2). It is this fully developed and quasi-steady stage that the present study is focused on.

To quantify the interactions between grid-scale and subgrid-scale motions, we define grid-scale motion as that obtained after applying a low-pass filter to the DNS data. In this study, the grid filter $\overline{G}(\boldsymbol{x})$ in (2.3) is defined as Gaussian filters (cf. Kwak,

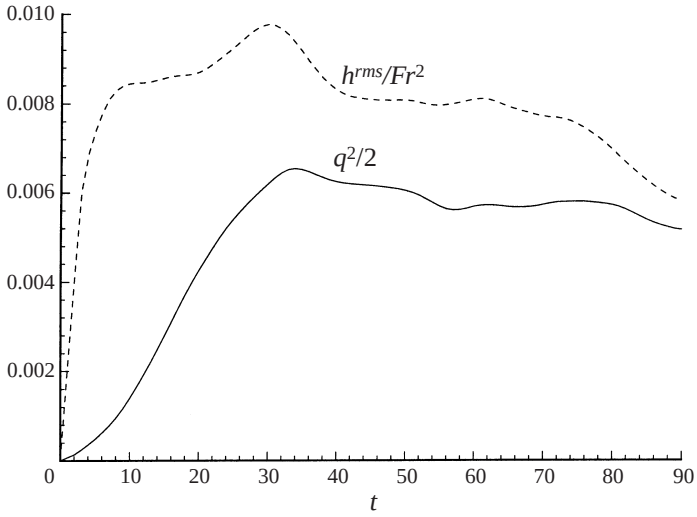

FIGURE 3. Time evolution of the free-surface turbulent kinetic energy $q^2|_{z=0}/2$ and the fluctuation of free-surface elevation h^{rms}/Fr^2.

Reynolds & Ferziger 1975) in the horizontal directions and a discrete filter in the vertical direction:

$$\left.\begin{aligned} \overline{G}(\boldsymbol{x}) &= \overline{G}_1(x)\overline{G}_2(y)\overline{G}_3(z), \\ \overline{G}_1(x) &= (6/\pi)^{1/2}\exp[-6x^2/\bar{\Delta}_x^2], \\ \overline{G}_2(y) &= (6/\pi)^{1/2}\exp[-6y^2/\bar{\Delta}_y^2], \\ \overline{G}_3(z) &= [\delta^D(z-\bar{\Delta}_z) + 2\delta^D(z) + \delta^D(z+\bar{\Delta}_z)]/4. \end{aligned}\right\} \tag{3.2}$$

Here δ^D is the Dirac delta function; and $\bar{\Delta}_x/\Delta_x = \bar{\Delta}_y/\Delta_y = 8$ and $\bar{\Delta}_z/\Delta_z = 2$ are the horizontal and vertical filter widths, respectively.

Figure 4 plots the horizontal energy spectrum $E_{u_iu_i}(k_n)$, which is defined as

$$E_{u_iu_i}(k_n;z) \equiv \sum_{k_n-\Delta_k/2\leqslant k<k_n+\Delta_k/2} \tfrac{1}{2}\widetilde{u}_i(k_x,k_y;z)\widetilde{u}_i^*(k_x,k_y;z)/\Delta_k, \quad i=1,2,3. \tag{3.3}$$

Here $k_n = n\Delta_k$, $n = 1, 2, 3\ldots$ with $\Delta_k = 2\pi/L_x = 2\pi/L_y$. In (3.3), $\widetilde{u}_i$ is the (horizontal) Fourier mode ($\widetilde{u}_i^*$ is the complex conjugate) of the velocity component u_i:

$$u_i(x,y,z,t) = \sum_{k_x,k_y} \widetilde{u}_i(k_x,k_y,z,t)\mathrm{e}^{\mathrm{i}k_x x}\mathrm{e}^{\mathrm{i}k_y y}, \tag{3.4}$$

where

$$k_x = n_x\Delta_k, \quad k_y = n_y\Delta_k, \quad \text{and} \quad k \equiv \sqrt{k_x^2+k_y^2}, \tag{3.5}$$

$$n_x = -N_x/2,\ldots,N_x/2-1, \quad n_y = -N_y/2,\ldots,N_y/2-1, \tag{3.6}$$

with $N_x(N_y)$ the grid numbers in the x- (y-) direction.

Because of the low Reynolds number limited by the DNS, only a relatively small portion of the energy spectrum $E_{u_iu_i}$ in figure 4 is close to the $k^{-5/3}$ high-wavenumber asymptote. Figure 4, however, shows clearly the overlap among the grid-scale portion of the kinetic energy, $E_{\bar{u}_i\bar{u}_i} \equiv \sum \widetilde{\bar{u}}_i\widetilde{\bar{u}}_i^*/(2\Delta_k)$, the subgrid-scale portion of the energy, $E_{u_i'u_i'} \equiv \sum \widetilde{u_i'}\widetilde{u_i'}^*/(2\Delta_k)$, and the remaining cross-portion, $E_{\bar{u}_iu_i'} \equiv \sum(\widetilde{\bar{u}}_i\widetilde{u_i'}^* + \widetilde{u_i'}\widetilde{\bar{u}}_i^*)/(2\Delta_k)$.

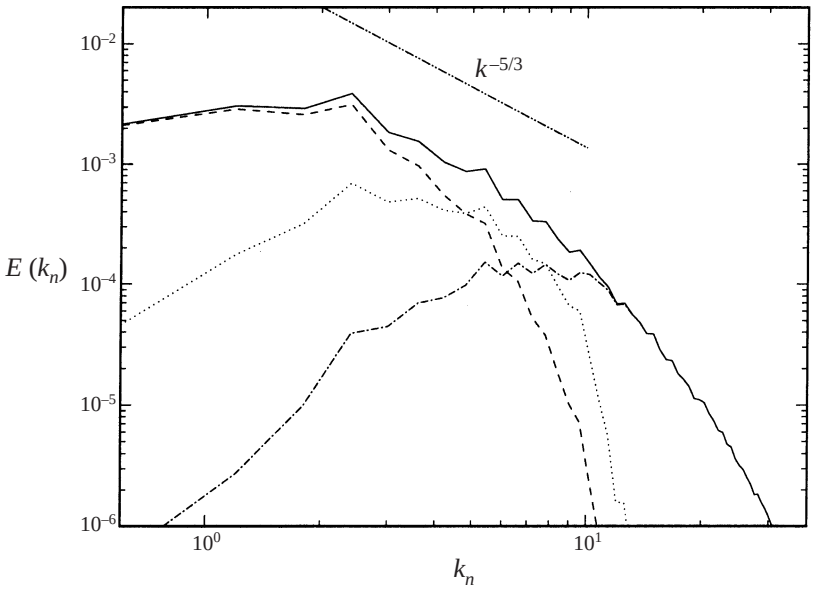

FIGURE 4. Kinetic energy spectra in the bulk flow ($z = -1.5$) for: the total velocity $E_{u_iu_i}$ (———); the grid-scale portion $E_{\bar{u}_i\bar{u}_i}$ (– – – –); the subgrid-scale portion $E_{u_i'u_i'}$ (– · – · –); and the cross-portion $E_{\bar{u}_iu_i'}$ (· · · · · ·). $t = 60$.

Such overlaps are a characteristic of the (horizontal) Gaussian filters (3.2). The use of the Gaussian filter and the resulting energy overlap are the basis of the scale-similarity SGS models. The importance of including such SGS models in the LES is demonstrated in simulations in § 4.6.

Similar to the energy spectrum, the turbulence kinetic energy $q^2/2$ itself can be separated into its scale components:

$$\tfrac{1}{2}q^2 \equiv \tfrac{1}{2}\langle (u_i - \langle u_i\rangle)^2\rangle = \underbrace{\tfrac{1}{2}\langle (\bar{u}_i - \langle \bar{u}_i\rangle)^2\rangle}_{\text{grid-scale component}} + \underbrace{\langle (\bar{u}_i - \langle \bar{u}_i\rangle)(u_i' - \langle u_i'\rangle)\rangle}_{\text{cross-contribution}} + \underbrace{\tfrac{1}{2}\langle u_i'^2\rangle}_{\text{subgrid-scale component}} . \tag{3.7}$$

Likewise, the Reynolds stress $\langle -uw\rangle$ can be separated as

$$\langle -uw\rangle = \underbrace{\langle -\bar{u}\,\bar{w}\rangle}_{\text{grid-scale component}} + \underbrace{\langle -\bar{u}w' - u'\bar{w}\rangle}_{\text{cross-contribution}} + \underbrace{\langle -u'w'\rangle}_{\text{subgrid-scale component}} . \tag{3.8}$$

Figure 5 plots the vertical profiles of these components for the turbulence energy and the Reynolds stress $\langle -uw\rangle$. It is clear that the grid-scale portion, which contains most of the energy, is responsible for the main part of the turbulence transport.

3.2. *Inter-scale energy transfer*

Turbulence is characterized by the energy cascade throughout different length scales. The most important role of the SGS model is to account for the energy transfer between the resolved and subgrid scales. Figure 6(*a*) plots the horizontal plane-averaged energy transfer $\langle \epsilon\rangle$ from the grid scales to the subgrid scales, where $\epsilon \equiv \tau_{ij}\bar{s}_{ij}$ and $\bar{s}_{ij} \equiv (\partial\bar{u}_i/\partial x_j + \partial\bar{u}_j/\partial x_i)/2$. Positive/negative sign of ϵ corresponds to energy transfer to/from the grid scales from/to the subgrid scales. From the figure, it is seen that the average energy transfer is from grid to subgrid scales at all depths. The amount of energy transferred into the subgrid scales is however much reduced near

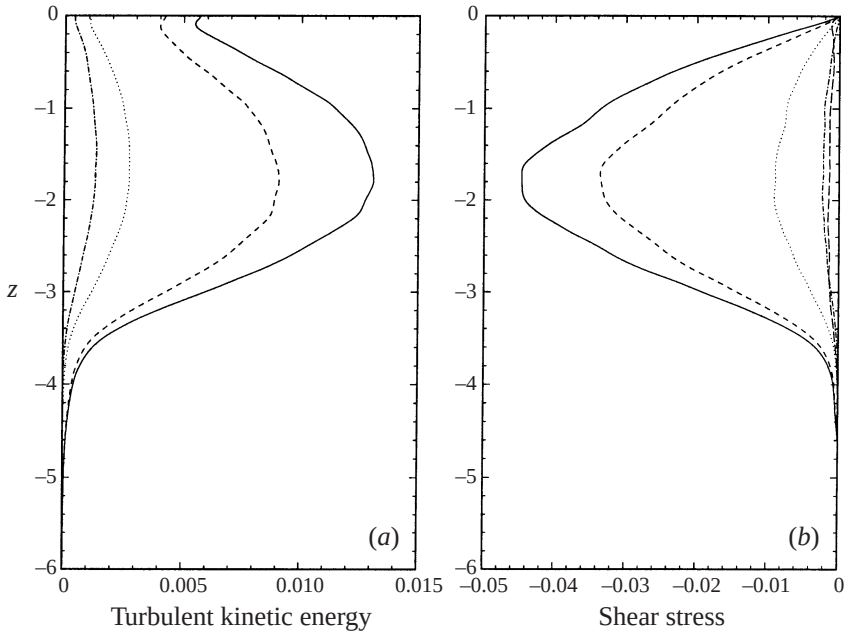

FIGURE 5. Profiles of the scale components of (*a*) turbulent kinetic energy $q^2/2$, and (*b*) Reynolds stress $\langle -uw \rangle$: ———, total; – – – –, grid-scale component; · · · · · ·, cross contribution; – · – · –, sub-grid-scale component. For reference, the viscous stress $Re^{-1}\partial\langle u\rangle/\partial z$ (—— ——) is also plotted in (*b*). $t = 60$.

the free surface. For example, in the Smagorinsky model of the SGS stress,

$$\tau_{ij} - \tfrac{1}{3}\delta_{ij}\tau_{kk} = -2C_S\bar{\Delta}^2|\bar{s}|^2\bar{s}_{ij}, \tag{3.9}$$

the coefficient C_S will, as a result, decrease towards the free surface. This behaviour of C_S is confirmed and shown in figure 6(*a*). In figure 6(*a*), C_S is obtained by assuming it to be constant in the horizontal plane and then calculated by best matching the two sides of (3.9) (cf. *a priori* tests by Clark, Ferziger & Reynolds 1979, and McMillan, Ferziger & Rogallo 1980). The overall filter width $\bar{\Delta}$ is set to be

$$\bar{\Delta} \equiv (\bar{\Delta}_x\bar{\Delta}_y\bar{\Delta}_z)^{1/3} = 0.2992. \tag{3.10}$$

Figure 6(*b*) plots the grid percentages at each horizontal plane where forward transfer (negative ϵ) or backward transfer (positive ϵ) occurs. In the bulk flow below, about 70% of the grids transfer energy forward while the remaining 30% experience energy backscatter. The relatively high percentage of backscatter is consistent with previous studies. Piomelli *et al.* (1991) found that for turbulent channel flow, backscatter occurs at nearly 50% of the points in the flow when a Fourier cutoff filter is used; if a Gaussian filter is used, the backscatter fraction is reduced to 30%. Of significant importance to the study of free-surface turbulence is the near-surface behaviour in figure 6(*b*) showing that the percentage of backscatter area increases from 30% to more than 40% as the free surface is approached.

The above results suggest that the inter-scale energy transfer near the free surface is significantly different from that in the bulk flow below and that energy backscatter must play a more important role near the surface. To further investigate these mechanisms, we study the energy cascade in the spectral space.

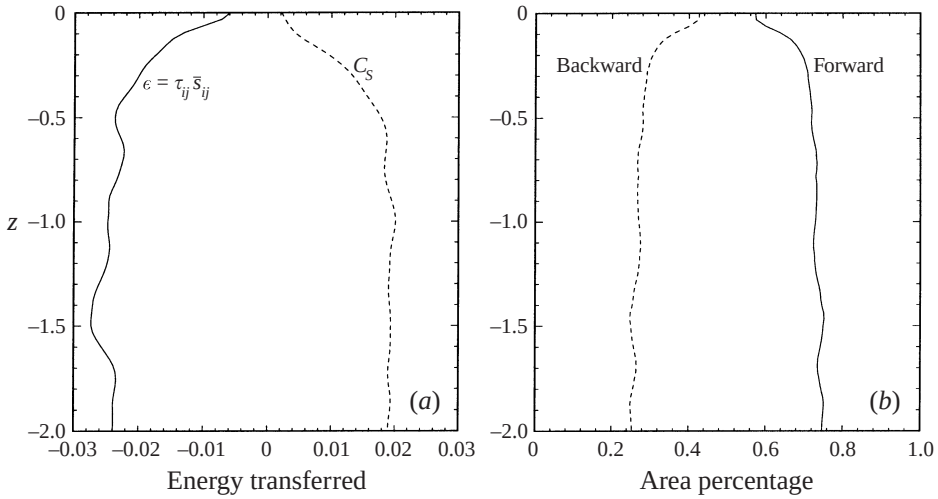

FIGURE 6. (*a*) Vertical variation of the energy transferred from the grid scales to the subgrid scales $\langle\epsilon\rangle$ (———) and the Smagorinsky coefficient C_S (– – – –). ϵ is normalized by the local turbulence kinetic energy $q^2(z)/2$. (*b*) Area percentages of grid points experiencing forward (grid to subgrid) transfer (———) and backward (subgrid to grid) transfer (– – – –). $t = 60$.

We denote the nonlinear advective terms as

$$\mathcal{N}_i \equiv -\frac{\partial u_i u_j}{\partial x_j}, \quad i = 1, 2, 3, \tag{3.11}$$

and the corresponding Fourier modes $\widetilde{\mathcal{N}}_i$. From (2.1) and (3.3), the effect of the nonlinear terms on $\partial E(k_n)/\partial t$ can be written as

$$\mathcal{T}(k_n) = \sum_{k_n - \Delta_k/2 \leqslant \sqrt{k_x^2 + k_y^2} < k_n + \Delta_k/2} \mathrm{Re}\{\widetilde{u}_i^*(k_x, k_y)\widetilde{\mathcal{N}}_i(k_x, k_y)\}/\Delta_k, \tag{3.12}$$

where Re denotes the real part.

The wave vector of the quadratic nonlinear terms, (k_x, k_y), and those of the two velocity components in the nonlinear terms, (k_x^r, k_y^r) and (k_x^s, k_y^s), must satisfy the following triangular relation:

$$(k_x, k_y) = (k_x^r, k_y^r) + (k_x^s, k_y^s). \tag{3.13}$$

In other words, it is the interaction between the two wavenumbers, $k^r = \sqrt{(k_x^r)^2 + (k_y^r)^2}$ and $k^s = \sqrt{(k_x^s)^2 + (k_y^s)^2}$, that results in the change at the third wavenumber $k = \sqrt{(k_x)^2 + (k_y)^2}$. For later reference, we use $\mathcal{T}^{k^r, k^s}(k)$ to denote the contribution to $\mathcal{T}(k)$ due to the quadratic interactions of the flow at two different wavenumbers k^r and k^s. To understand the contributions from the different scales, it is convenient to partition the k^r, k^s domain into different wavenumber regimes: k^r, $k^s \in$ M, I, II, III, A. These correspond to the regimes: M $= \{k\colon\ k = 0\}$ (mean flow); I $= \{k\colon\ 0.6 \leqslant k < 5.4\}$ (large scales); II $= \{k\colon\ 5.4 \leqslant k < 10.2\}$ (small resolved scales and large subgrid scales); III $= \{k\colon\ 10.2 \leqslant k < 15\}$ (small scales); and A $= \{k\colon\ k > 0\}$ (all turbulent fluctuation wavenumbers). For each of these energy transfer terms, we further define their directional components, $\mathcal{T}_j^{k^r, k^s}$, $j = x, y, z$, which correspond to the contributions

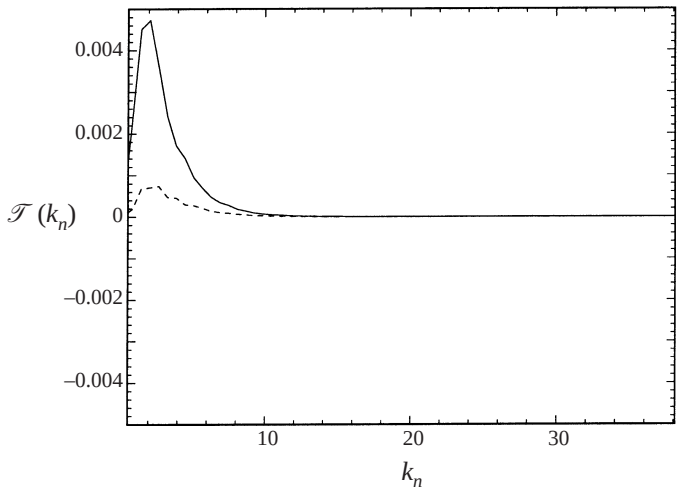

FIGURE 7. Energy transferred from the mean flow to all the scales of turbulent fluctuations $\mathscr{T}^{M,A}$: ———, deep region; – – – –, free surface.

to $\mathscr{T}^{k^r,k^s}$ due to the jth component of the advection term, $-\partial u_i u_j/\partial x_j$ (no summation for j).

We first consider the interaction between the mean flow and the total turbulent fluctuations, $\mathscr{T}^{M,A}$. This is plotted in figure 7 for the free-surface region (averaged over $-0.25 \leqslant z \leqslant 0$) and the deep region (averaged over $-1.625 \leqslant z \leqslant -1.375$). Here and hereafter, $\mathscr{T}$ is normalized by the local turbulent kinetic energy $q^2(z,t)/2$. Figure 7 shows clearly the energy extraction from the mean flow to turbulent fluctuations and that it is the low wavenumbers (largest eddies) that receive most of the energy directly. Figure 7 also shows that the turbulent production near the free surface is much less than that in the deep region. This is consistent with Shen *et al.* (1999) who considered the total production $\langle -uw\rangle \partial\langle u\rangle/\partial z$ in the physical space. This reduction was explained by Shen *et al.* (1999) through two mechanisms: (i) the annihilation of w due to the constraint on the vertical motion at the free surface; and (ii) the vanishing of $\partial\langle u\rangle/\partial z$ caused by the shear-free free-surface boundary condition.

Next we investigate the interaction among the total turbulent fluctuations, $\mathscr{T}^{A,A}$, which is plotted in figure 8(a). The forward energy transfer (for the low wavenumbers) is manifested in the bulk region, as expected. This energy transfer is, however, very different near the free surface where it is predominately one of backscattering (although at a smaller magnitude). This reverse energy transfer mechanism near the free surface is consistent with the finding in figure 6 and was also observed in free-surface jet flows (e.g. Mangiavacchi, Gundlapalli & Akhavan 1994).

The overall picture is clarified if we consider the contributions to $\mathscr{T}^{A,A}$ from the different wavenumber scales, specifically: $\mathscr{T}^{I,A}$, $\mathscr{T}^{II,A}$, $\mathscr{T}^{III,A}$. These are plotted in figures 8(b), 8(c), and 8(d), respectively. From these figures, we observe that, in the bulk region, the role of each band is to remove the energy from the larger scales to the smaller scales. This is in agreement with the previous studies on other types of flows (see e.g. Domaradzki & Rogallo 1990 for isotropic homogeneous turbulence, and Domaradzki *et al.* 1994 for wall-bounded turbulence). Near the free surface, band I (large scales) feeds energy into the low wavenumbers, similar to the backscatter shown in figure 8(a), while the intermediate and small scales, bands II and III, continue to transfer energy forward. Nevertheless, the magnitudes of the forward energy transfer

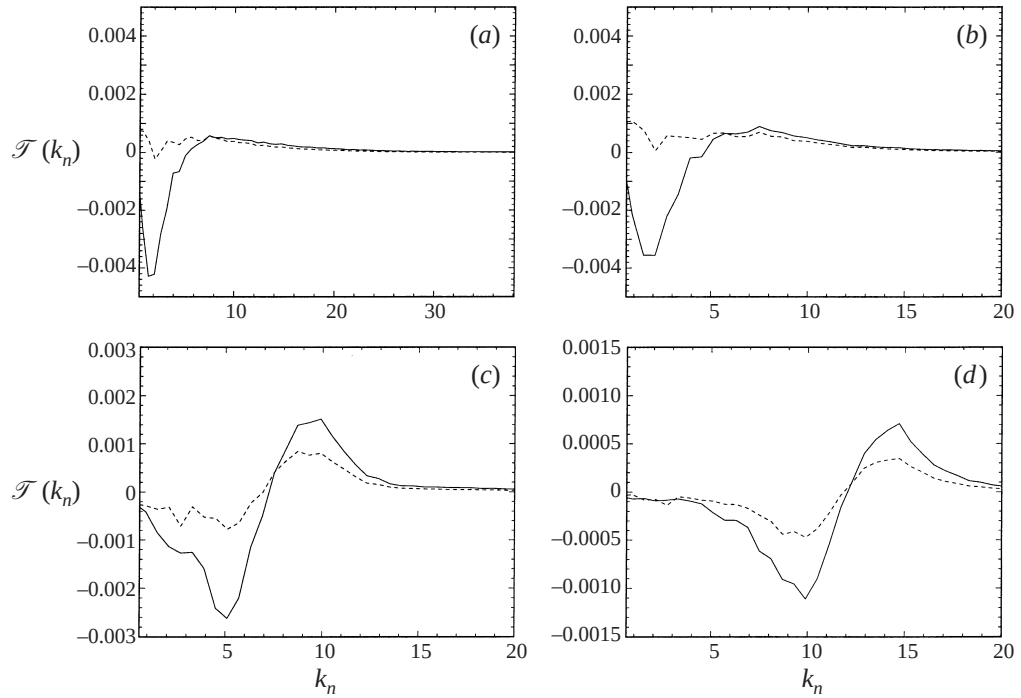

FIGURE 8. Inter-scale energy transfer: (*a*) among the turbulent fluctuations total $\mathscr{T}^{A,A}$; and associated with (*b*) band I ($0.6 \leqslant k < 5.4$) $\mathscr{T}^{I,A}$, (*c*) band II ($5.4 \leqslant k < 10.2$) $\mathscr{T}^{II,A}$, and (*d*) band III ($10.2 \leqslant k < 15$) $\mathscr{T}^{III,A}$. ———, Deep region; – – – –, free surface.

by bands II and III near the free surface are much less than the corresponding values in the bulk.

More insight into the inter-scale energy transfer can be obtained by considering the directional components of $\mathscr{T}_j$. It is found that for $j = x$ and y, the difference between $\mathscr{T}$ in the bulk and at the free surface is insignificant: in both cases, energy is transferred from larger to smaller scales (results not plotted here). It is for the vertical component $\mathscr{T}_z$ (figure 9) that fundamental differences obtain between the bulk and free surface: the forward energy transfer in the bulk becomes negative and is comparable in magnitude at the free surface. Clearly this reversal is related to the vertical convective velocity term:

$$-\frac{\partial u_i w}{\partial z} = -w\frac{\partial u_i}{\partial z} - u_i\frac{\partial w}{\partial z}, \quad i = 1, 2, 3. \tag{3.14}$$

The vertical velocity w is small near the free surface and hence the second term $-u_i\partial w/\partial z$ dominates. Since $\partial w/\partial z = -(\partial u/\partial x + \partial v/\partial y)$ measures the divergence at the horizontal plane, we conjecture that the energy backscatter in free-surface turbulence is probably related to the splat and antisplat motions near the surface. This is confirmed in § 3.3.

In summary, it is found that the mechanism of inter-scale energy transfer near a free surface is substantially different from that in the bulk flow. The typical energy cascade from large to small scales does not obtain near the free surface. This energy backscatter, which is found to be caused by vertical convection, plays a prominent role in the structure of free-surface turbulence.

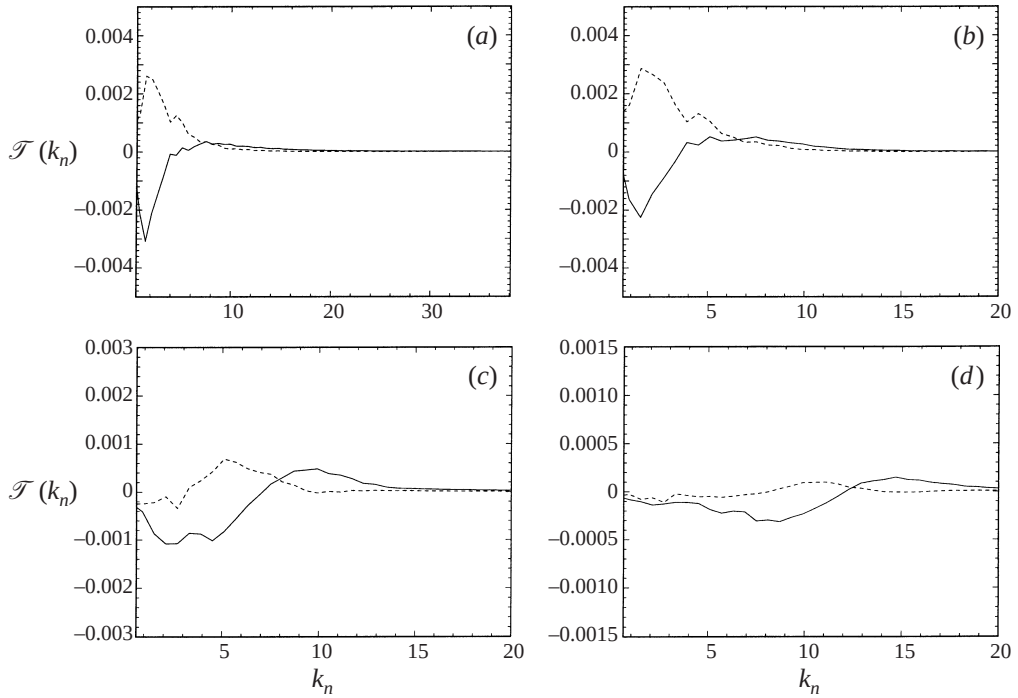

FIGURE 9. Contribution from z-advection to inter-scale energy transfer: (a) among the turbulent fluctuations total $\mathscr{T}_z^{A,A}$; and associated with (b) band I ($0.6 \leqslant k < 5.4$) $\mathscr{T}_z^{I,A}$, (c) band II ($5.4 \leqslant k < 10.2$) $\mathscr{T}_z^{II,A}$, and (d) band III ($10.2 \leqslant k < 15$) $\mathscr{T}_z^{III,A}$. ———, Deep region; – – – –, free surface.

3.3. *Coherent vortical structures at the free surface*

The reverse inter-scale energy transfer in free-surface turbulence is related to the presence of coherent vortex structures at the surface. The correlation between the turbulent structures and the forward/backward inter-scale energy transfer has received some attention in recent years. Hartel *et al.* (1994) showed that the backscatter near a solid wall is strongly enhanced by coherent motions such as bursting events. Piomelli, Yu & Adrian (1996) investigated the dependence of the inter-scale energy transfer on the large-scale turbulent structures in wall-bounded flows. These studies of wall-bounded flows provide important physical insights for the development of SGS models. For free-surface turbulence in an open-channel flow, Pan & Banerjee (1995) found strong backscatter in the upwellings, while strong forward energy transfers are at the outskirts of the surface-connecting vortices where the shear is high. The energy transfers at the vortex core regions are found to be weak. These features are also obtained in our present simulations (results not shown here).

From earlier studies (cf. Shen *et al.* 1999) it is shown that free-surface shear turbulence is characterized by the presence of hairpin vortices which are inclined with the mean flow with head portions near the free surface and the two legs extending into the bulk region. As a hairpin vortex approaches the surface, the head portion is dissipated quickly within a surface layer and the two legs connect to the surface, resulting in a pair of persistent counter-rotating surface-connected vortices. (These processes are studied in some detail by Shen *et al.* 1999.) In our SGS modelling, we find that it is essential to capture the inter-dependence of near-surface vortex dynamics and inter-scale energy transfer in order to obtain adequate prediction of the surface signature.

To analyse the coherent turbulent structures, we employ the method of conditional averaging (see Antonia 1981 for a review of this method for turbulence studies). Specifically, we use a variable-interval space-averaging (VISA) technique (Kim 1983; Hartel *et al.* 1994; Piomelli *et al.* 1996), which is based on the variable-interval time-averaging (VITA) method developed by Blackwelder & Kaplan (1976). We summarize the VISA procedure used in the present study as follows. The event we want to capture is the head portion of the hairpin vortex near the free surface, i.e. large negative spanwise vorticity ω_y. Its variable-interval space averaging is defined as

$$\underline{\omega}_y(x, y, z, t, W) \equiv \frac{1}{4W^2} \int_{x-W}^{x+W} \int_{y-W}^{y+W} \omega_y(\xi, \zeta, z, t) \mathrm{d}\xi \mathrm{d}\zeta, \tag{3.15}$$

where W is the half-width of the averaging window, which has a value about 1 (macroscale) in this study. To identify strong ω_y events, a localized variance is introduced:

$$\omega_y^{var}(x, y, z, t, W) \equiv \omega_y^2(x, y, z, t) - \underline{\omega}_y^2(x, y, z, t, W). \tag{3.16}$$

Strong hairpin head events are detected using the following criterion:

$$\mathscr{D}(x, y, z, t) = \begin{cases} 1 & \text{if} \quad \omega_y^{var} > c(\omega_y^{rms})^2, \\ 0 & \text{otherwise.} \end{cases} \tag{3.17}$$

Here the detection function $\mathscr{D}(x, y, z, t) = 1$ if the hairpin head exists; ω_y^{rms} is the root-mean-square variation of ω_y at the horizontal plane; and c is the threshold level, which has the value 15 in the present study. We use the data from $t = 40$ to 90 from 25 DNS realizations averaging over $O(1000)$ events. The three-dimensional flow field associated with each event is then ensemble averaged to yield the VISA field. (Before the averaging, the coordinates are transformed horizontally so that all the events are centred at $(0, 0, z_d)$.) In this study, we have investigated hairpin head events at horizontal planes of difference depths z_d ranging from $z_d = -0.25$ to -0.0625. Increasing z_d corresponds to later phases of the vortex connection process (cf. Shen *et al.* 1999). For conciseness, in this paper we only show the representive case with $z_d = -0.125$.

Figure 10 shows an example of the resulting VISA flow field. The averaged hairpin head is centered at $(0, 0, -0.125)$ in the plots. Figure 10(*a*) shows the isosurface of the vorticity magnitude $|\boldsymbol{\omega}|$. The head portion and the two legs of the hairpin are seen with the legs inclined with the mean shear flow (cf. figure 1).

One of the major findings of this study is shown in figure 10(*b*), where the region with energy backscatter is plotted. Comparing figures 10(*a*) and 10(*b*), it is seen that there is a distinct region of backwards energy transfer (positive $\tau_{ij}\bar{s}_{ij}$) downstream of the hairpin structure. The remainder of this sub-section is devoted to elucidating this feature.

Figure 11 plots vertical (x,z) sections at the centre ($y = 0$) of the VISA hairpin vortex. Owing to the induction of the hairpin head (which has negative ω_y component) and the two hairpin legs, the fluid downstream is advected to the free surface ('splats'), while the fluid upstream moves away from the free surface ('antisplats'). The contours of the SGS dissipation in figure 11 show clearly the energy backscatter (positive $\tau_{ij}\bar{s}_{ij}$) region located downstream of the hairpin vortex. The thickness of this region is about 0.1 and is comparable to the thickness of the surface layer identified in Shen *et al.* (1999, 2000).

The surface characteristics of the VISA field are of immediate interest, and are plotted in figure 12. The surface contours of the spanwise vorticity, ω_y, (part *a*),

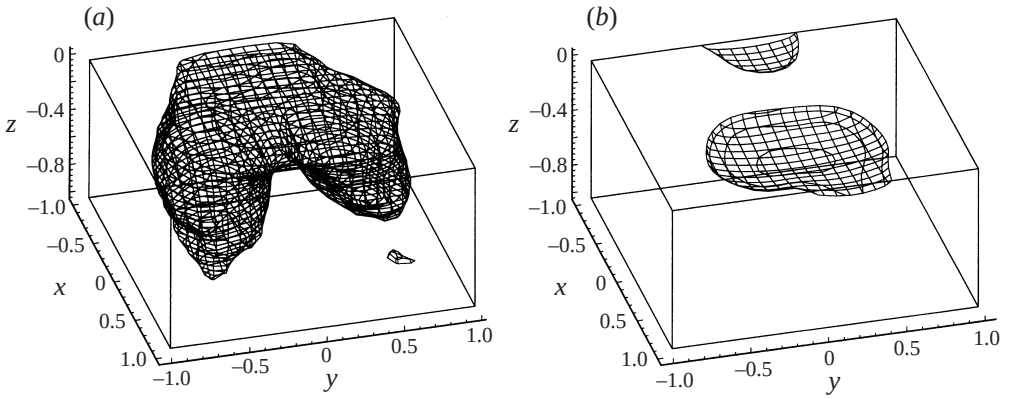

FIGURE 10. Coherent hairpin vortex structure in the conditionally averaged VISA flow field: (*a*) region where vorticity magnitude $|\boldsymbol{\omega}| \geqslant 0.2$; and (*b*) region where SGS dissipation $\tau_{ij}\bar{s}_{ij} \geqslant 0$ (energy backscatter). The mean flow is in the positive x-direction.

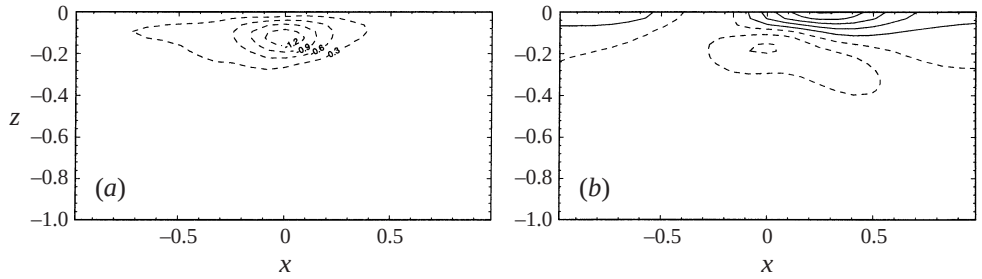

FIGURE 11. Vertical centreplane ($y = 0$) sections of the VISA hairpin structure: (*a*) the contours of ω_y; (*b*) the contours of $\tau_{ij}\bar{s}_{ij}$ with contour interval 0.0002. Dashed lines represent negative values. The mean flow is in the positive x-direction.

which is induced by the primary vortex beneath, show that the surface vorticity is positive in the centre region (the hairpin head has negative ω_y) and negative at the two sides. From the surface-normal vorticity ω_z (part *b*), it is seen that as the hairpin vortex approaches the surface, positive/negative ω_z appears upstream on both sides of the symmetry plane ($y = 0$). These eventually evolve into a pair of counter-rotating surface-connected vortices.

Surface contours of SGS dissipation $\tau_{ij}\bar{s}_{ij}$ are plotted in figure 12(*c*). The energy backscatter in the downstream region is clearly seen. Figure 12(*d*) plots contours of the Smagorinsky coefficient C_S obtained by matching the model (3.9) point by point with the DNS-resolved SGS stresses. As expected, $C_S < 0$ in the region of energy backscatter.

According to Shen *et al.* (1999), the inclination angle of the vorticity at the surface, $\alpha \equiv \tan^{-1}\left(\sqrt{\omega_x^2 + \omega_y^2}/|\omega_z|\right)$, is a good indicator of the temporal phase or 'age' of a surface-connecting hairpin vortex. During the connection, α is large ($\gtrsim 25^\circ$), as shown in figure 12(*e*). After connection, ω_z becomes dominant while ω_x and ω_y are dissipated and α becomes small ($\lesssim 5^\circ$ in the present case). The detailed results for this latter condition are not shown here but were discussed extensively in Shen *et al.* (1999). It was found that surface-connected vorticity is persistent and decays at a slow rate (more comparable to a laminar condition). This is in agreement with Pan

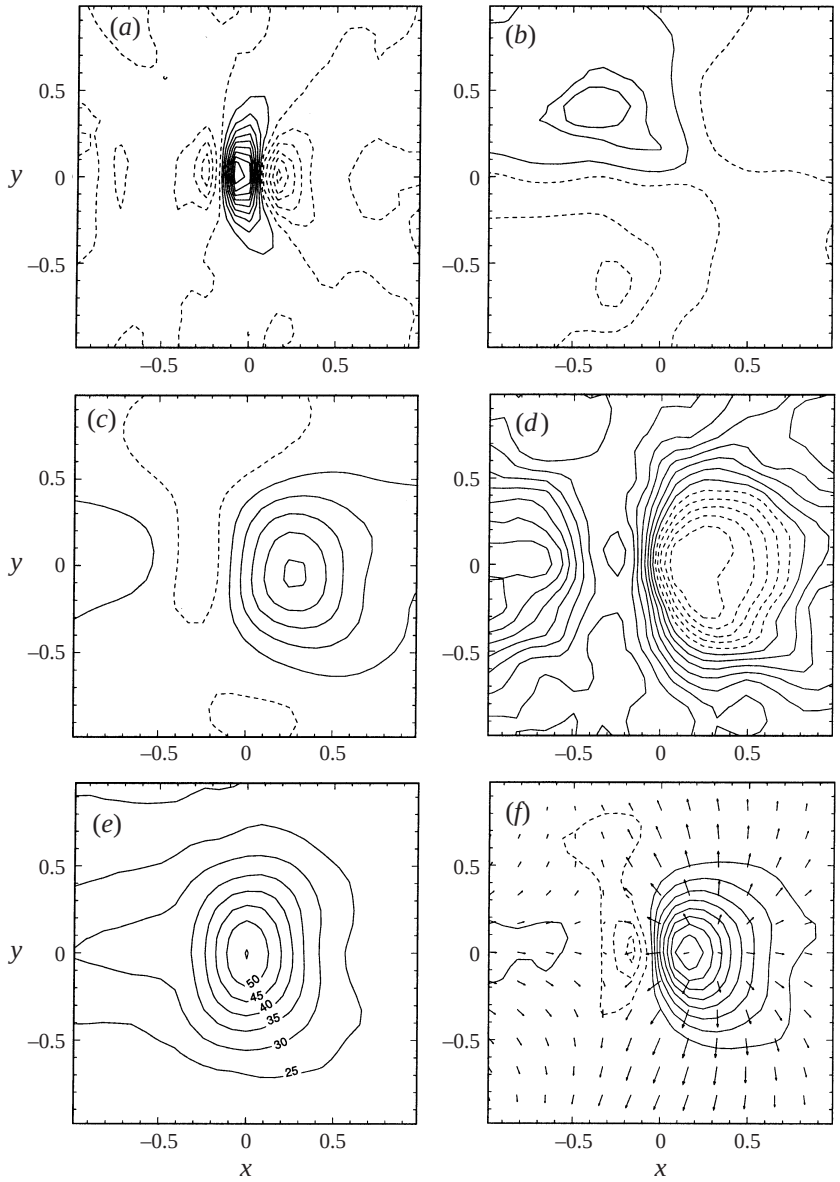

FIGURE 12. VISA surface features above the hairpin vortex: contours of (*a*) ω_y with contour interval 0.01; (*b*) ω_z with contour interval 0.05; (*c*) $\tau_{ij}\bar{s}_{ij}$ with contour interval 0.0002; (*d*) C_S with contour interval 0.001; (*e*) α; and (*f*) $\partial u/\partial x + \partial v/\partial y$ with contour interval 0.05 and the fluctuation velocity vectors $(u - \langle u \rangle, v - \langle v \rangle)$. Dashed lines represent negative values.

& Banerjee (1995) who observed that the energy cascade magnitude is small at the cores of surface-connected vortices.

Finally, figure 12(*f*) plots the horizontal divergence $\partial u/\partial x + \partial v/\partial y = -\partial w/\partial z$ together with the horizontal velocity fluctuation vectors $(u - \langle u \rangle, v - \langle v \rangle)$. These show clearly the regions of splats and antisplats. The downstream splat region, when compared with figures 12(*c*) and 12(*d*), is shown to correlate directly with the region of energy backscatter.

In summary, conditional averaging shows that energy backscatter at the free surface occurs at the downstream splat region of coherent hairpin structures approaching the surface. This region is also characterized by large vortex inclination angles (relative to the vertical) and positive horizontal velocity divergence $\partial u/\partial x + \partial v/\partial y$. The physics revealed herein is used directly in our later development of SGS stress models for free-surface turbulence in § 4.

3.4. *Anisotropy in the surface layer*

In some sense, a necessary difference between isotropic turbulence and free-surface turbulence is anisotropy of the latter due to the imposition of kinematic and dynamic boundary conditions at the free surface (cf. e.g. Shen *et al.* 1999). Figure 13 plots the vertical profiles of the velocity and vorticity components in the three wavenumber bands I, II, and III. The anisotropy in the velocity is a direct consequence of the kinematic free-surface condition which renders w much smaller than u and v near the free surface. The anisotropy in the velocity gradients is caused by the vanishing tangential-stress free-surface boundary conditions which results in horizontal vorticity components ω_x and ω_y much smaller than the vertical component ω_z. Comparing the results for the different wavenumber bands, it is significant that the free-surface anisotropy remains qualitatively undiminished for different eddy wavenumbers. Thus, anisotropy is an essential feature that must be accounted for by free-surface turbulence SGS models.

Figure 13 also reveals the vertical extents of the free-surface anisotropy regions as eddy wavenumber increases. To examine this further, we compare the normalized (by values in the bulk) vertical profiles for different wavenumber bands. Figure 14 plots typical results for w and ω_x. As a measure of the respective surface layer thickness, the point at which maximum (negative) curvature occurs on each profile is also indicated. For the velocity, the thickness generally decreases with increasing k as expected from physical reasoning. For ω_x (a similar result obtains for ω_y), there is little variation of the anistropy thickness with wavenumber, and the overall thickness is smaller than those for the velocity components, consistent with the respective inner versus outer (blockage) layer effects they manifest.

The double-layer structure near the free surface is elucidated by considering the vertical variation of the (horizontally averaged) turbulence diffusivity. This is done in Shen *et al.* (2000) where it is found that the surface layer is characterized by a rapid reduction of the turbulence diffusivity. This behaviour is fitted well by a Guassian profile and can be modelled by an analytical similarity solution for the mean flow. Of special relevance here is the fact that the outer and inner layer structure of the free-surface boundary layer can be quantified in terms of the mean flow profile. In particular, the outer and inner thicknesses are given by the local minimum and then the local maximum of the shear profile as the surface is approached (cf. figure 26).

We now examine the extent of anisotropy in the SGS stress. Figure 15 plots the depth variation of the r.m.s. values of the (trace-free) SGS stress and the (grid-scale) strain rate components. As expected, there is significant anisotropy near the free surface: for both the SGS stress and strain rate, the 'horizontal' components $ij = 11$, 12, 22, 33 increase towards the free surface, while the 'vertical' components $ij = 13$, 23 decrease. Note that $ij = 33$ is also a 'horizontal' component because w and thus $\tau_{33} \equiv \overline{ww} - \bar{w}\,\bar{w}$ is small near the free surface, so that $\tau_{33} - \tau_{kk}/3$ contains mainly contributions from τ_{11} and τ_{22}. We notice, however, that the extents over which the anisotropic variations occur are quite different for the stress versus the strain rate. The reason is that the anisotropy in the SGS stress is a direct result of the kinematic constraint on the vertical motion, while that in the strain is due to the dynamic

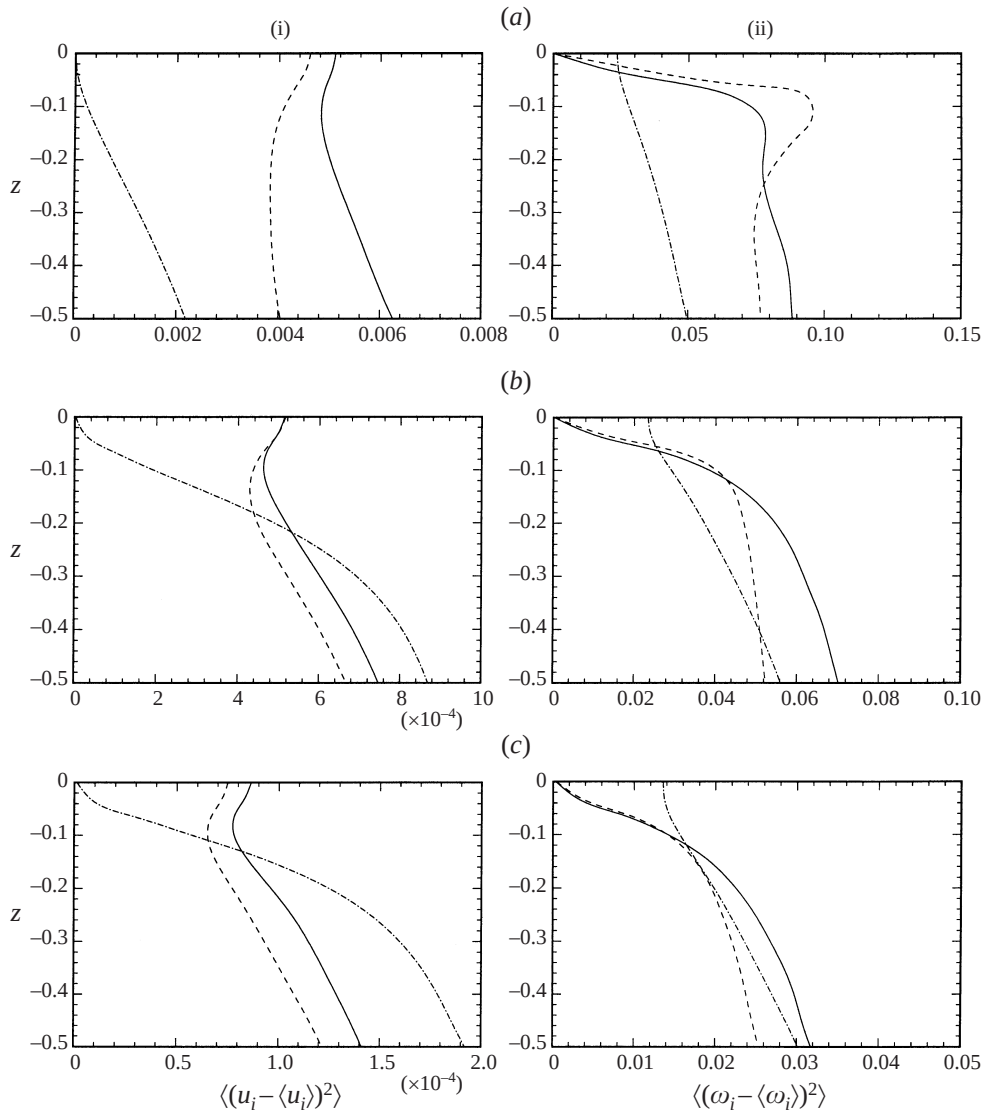

FIGURE 13. Vertical profiles of the turbulence fluctuation of (i) velocity and (ii) vorticity x- (———), y- (– – – –) and z-components (– · – · –); in wavenumber bands: $k \in$ (*a*) I; (*b*) II; and (*c*) III. $t = 60$.

condition of vanishing tangential stresses. Consequently, the SGS stress varies within a 'blockage' layer which is much thicker than the 'inner' layer over which the strain rate varies (cf. Shen *et al.* 1999).

A useful way to measure the correlation between the SGS stress and strain rate is to consider *a priori* tests of a standard eddy-viscosity SGS (Smagorinsky) model (3.9). If we assume the Smagorinsky coefficient C_S to be constant horizontally but a function of depth, it can be determined *a priori* as in figure 6. The goodness of fit of this model is measured by the correlation coefficient between the trace-free SGS stress and the SGS model:

$$\mathrm{Cor}(z,t) \equiv \frac{\langle(\tau_{ij} - \delta_{ij}\tau_{kk}/3 - \langle\tau_{ij} - \delta_{ij}\tau_{kk}/3\rangle)(M_{ij} - \langle M_{ij}\rangle)\rangle}{(\tau_{ij} - \delta_{ij}\tau_{kk}/3 - \langle\tau_{ij} - \delta_{ij}\tau_{kk}/3\rangle)^{rms}(M_{ij} - \langle M_{ij}\rangle)^{rms}}. \tag{3.18}$$

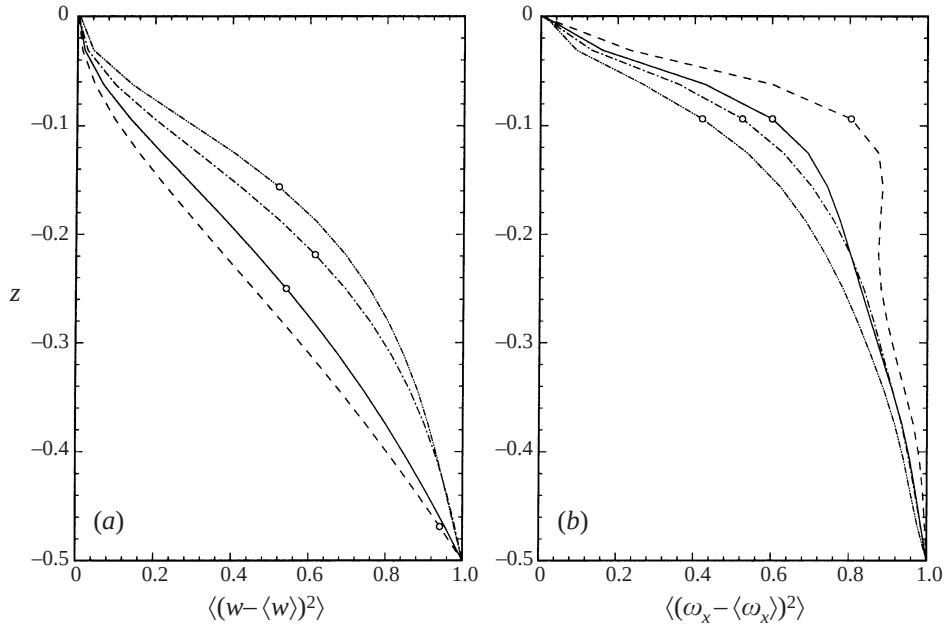

FIGURE 14. Normalized vertical profiles of the turbulence fluctuation: (*a*) vertical velocity w; and (*b*) streamwise vorticity ω_x; in wavenumber bands: $k \in$ I (– – – –); II (– · – · –); III (– ·· – ·· –) and A (———). $t = 60$. The profiles are normalized by the bulk values. The point of maximum (negative) curvature on each curve is indicated by ○.

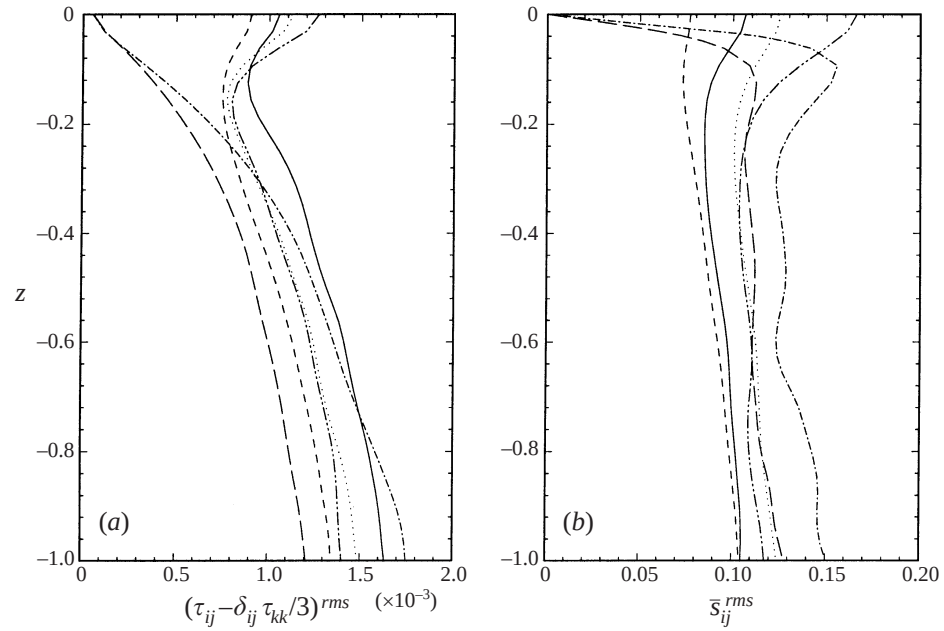

FIGURE 15. Vertical variation of the magnitudes of the different components of (*a*) trace-free SGS stress $(\tau_{ij} - \delta_{ij}\tau_{kk}/3)^{rms}$ and (*b*) strain rate $\bar{s}_{ij}^{rms}$. ———, $ij = 11$; – – – –, $ij = 12$; – · – · –, $ij = 13$; · · · · · ·, $ij = 22$; — — —, $ij = 23$; – ·· – ·· –, $ij = 33$. $t = 60$.

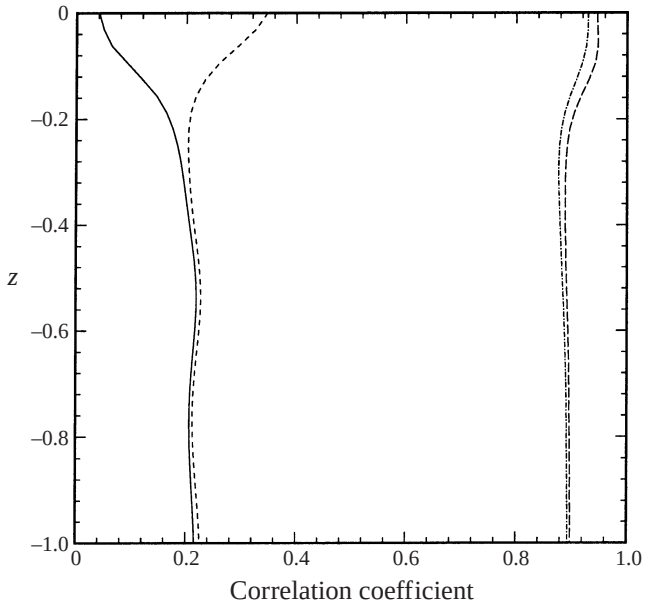

FIGURE 16. Correlation coefficient (3.18) between the trace-free SGS stress $\tau_{ij} - \delta_{ij}\tau_{kk}/3$ and: ———, dynamic Smagorinsky model (DSM); – – – –, dynamic anisotropic selective model (DASM); –·–·–, DSM combined with a scale-similarity model (DSM+B); — —, DASM combined with a scale-similarity model (DASM+B). $t = 60$.

This is plotted in figure 16 (the model is labelled 'DSM'). In the bulk flow, the correlation coefficient is about 0.2. This is in agreement with previous studies on other types of turbulent flows (see e.g. Clark *et al.* 1979; McMillan *et al.* 1980; Liu, Meneveau & Katz 1994). The reason for the low correlation between the actual SGS stress and the Smagorinsky model is that their principal axes are not aligned. Near a free surface, the correlation drops even lower. Clearly, a dynamic Smagorinsky model is not an effective model for free-surface turbulence.

Armed with these physical observations, we now proceed to the development of effective SGS modelling and LES of free-surface turbulence.

4. Development of LES for free-surface turbulence

As pointed out in § 2, in addition to the need to model the SGS stress in the momentum equations, the imposition of free-surface boundary conditions introduces additional SGS quantities associated with the isotropic dynamic pressure $p_{SGS} \equiv \tau_{kk}/3$ and SGS flux $\tau_{u,v}^{kbc}$. The models we use for these free-surface SGS quantities are discussed in § 2.2.

From the analysis of DNS data in § 3, we obtained physical insights into free-surface turbulence which should be captured in LES: (i) As the free surface is approached, the energy transfer from large scales to small scales decreases significantly. This reduction is caused by the presence of energy backscatter associated with the vertical motions near the free surface. (ii) The inverse energy transfer is strongly correlated with the coherent (hairpin) vortex structures in the near-surface region which are characteristic of free-surface shear flows. In particular, strong backscatter is found to occur in the splat region associated with the connection of hairpin vortices to the free surface.

(iii) The turbulence field near the free surface is highly anisotropic. This anisotropy prevails as the length scales of the turbulence eddies decrease and is manifested as qualitatively different behaviours in different components of the SGS stress. As a result, the correlation between actual and modelled SGS stresses in traditional eddy-viscosity-type SGS models is quite poor.

In the following, a number of new SGS stress models for free-surface turbulence are introduced and compared with more standard approaches. The relative merits of these models tested against the DNS dataset are then presented and discussed.

4.1. *SGS stress models for free-surface turbulence*

In general, the SGS stress (2.8) can be modelled with or without splitting it into separate components, for example the Leonard stress, cross-stress and 'true' SGS stress; or the modified definitions suggested by Germano (1986). In this work, we adopt the approach where the SGS stress is treated as a whole (cf. Lesieur & Métais 1996). All the models we present satisfy Galilean invariance (cf. Speziale 1985).

The base model we use here is the plane-averaged dynamic Smagorinsky model (DSM), which we use to compare to two new SGS models: a dynamic anisotropic selective model (DASM), which captures the dependence of energy backscatter on the coherent vortex structure and the anisotropy nature of free-surface turbulence; and a dynamic free-surface function model (DFFM), which directly accounts for the variation of the eddy viscosity in the surface layer.

4.1.1. *Dynamic Smagorinsky model* (*DSM*)

We consider the dynamic formulation of the Smagorinsky model (3.9) following the procedure of Germano *et al.* (1991) with the modification of Lilly (1992). At the coarse filter $\hat{\overline{G}}$ level, the Smagorinsky model is written as

$$T_{ij} - \tfrac{1}{3}\delta_{ij}T_{kk} = -2C_S\hat{\bar{\Delta}}^2|\hat{\bar{s}}|^2\hat{\bar{s}}_{ij}. \tag{4.1}$$

The Germano identity states that

$$\mathscr{L}_{ij} - \tfrac{1}{3}\delta_{ij}\mathscr{L}_{kk} = T_{ij} - \widehat{\tau_{ij}} - \tfrac{1}{3}\delta_{ij}(T_{kk} - \widehat{\tau_{kk}}) = -2C_S\hat{\bar{\Delta}}^2|\hat{\bar{s}}|^2\hat{\bar{s}}_{ij} + (2C_S\widehat{\bar{\Delta}^2|\bar{s}|^2\bar{s}_{ij}}). \tag{4.2}$$

Assuming that C_S is constant over the horizontal plane and applying the test filter $\widehat{G}$ in the horizontal directions only, (4.2) reduces to

$$\mathscr{L}_{ij} - \tfrac{1}{3}\delta_{ij}\mathscr{L}_{kk} = C_S(2\widehat{\bar{\Delta}^2|\bar{s}|^2\bar{s}_{ij}} - 2\hat{\bar{\Delta}}^2|\hat{\bar{s}}|^2\hat{\bar{s}}_{ij}). \tag{4.3}$$

The coefficient C_S is chosen to best match the above equation on the horizontal plane using a least-square approach (Lilly 1992):

$$C_S(z,t) = \frac{\langle \mathscr{L}_{ij}m_{ij}\rangle}{\langle m_{ij}^2\rangle}. \tag{4.4}$$

Here $m_{ij} = 2\widehat{\bar{\Delta}^2|\bar{s}|^2\bar{s}_{ij}} - 2\hat{\bar{\Delta}}^2|\hat{\bar{s}}|^2\hat{\bar{s}}_{ij}$ and $\bar{s}_{kk} = \hat{\bar{s}}_{kk} = 0$ is used, which is based on continuity.

4.1.2. *Dynamic anisotropic selective model* (*DASM*)

The poor correlation between the Smagorinsky model and the SGS stress near the free surface in figure 16 can be attributed to the use of a single coefficient $C_S(z,t)$ for all the stress components in each entire horizontal plane. As pointed out earlier, the tangential components exhibit behaviour different from the other components because of the free-surface anisotropy, which may cause the principal axes of the model tensor

to be far from those of the actual SGS stress. In addition, the increase in backscatter near the free surface is also not accounted for by (3.9): when a single positive model coefficient is used, the correlation in the backscatter region is necessarily negative, which reduces the overall correlation.

For this highly anisotropic flow, it is useful to consider different model coefficients in (3.9) for the different SGS stress components:

$$\tau_{ij} - \tfrac{1}{3}\delta_{ij}\tau_{kk} = -2C_{ij}\bar{\Delta}^2|\bar{s}|\bar{s}_{ij}, \quad \text{no summation for } ij. \tag{4.5}$$

Since the flow is also highly varying in space (see e.g. the horizontal variations in figure 12), the (horizontal) spatial variation of C_{ij} is of interest.

Guided by the results of § 3 (e.g. figure 15), we propose to model C_{ij} in two separate groups: the vertical coefficients $ij = 13$, (31), 23, (32); and horizontal coefficients $ij = 11$, 12, (21), 22, 33. The expectation (this is confirmed by extensive direct *a priori* tests) is that the horizontal coefficients will be positive in regions of forward energy cascade and negative in regions with energy backscatter, while the vertical coefficients will not be much affected by the energy forward/backward transfer. It is then natural to propose an anisotropic SGS model which has different coefficients for the horizontal and vertical components:

$$\tau_{ij} - \tfrac{1}{3}\delta_{ij}\tau_{kk} = -2\bar{\Delta}^2|\bar{s}| \begin{pmatrix} C_H^n\bar{s}_{11} & C_H^n\bar{s}_{12} & C_V^n\bar{s}_{13} \\ C_H^n\bar{s}_{21} & C_H^n\bar{s}_{22} & C_V^n\bar{s}_{23} \\ C_V^n\bar{s}_{31} & C_V^n\bar{s}_{32} & C_H^n\bar{s}_{33} \end{pmatrix}. \tag{4.6}$$

As in DSM, the model coefficients are functions of depth and time, $C_H^n(z,t)$, $C_V^n(z,t)$, but the subscripts H and V correspond to 'horizontal' and 'vertical', respectively. In addition to the anisotropy, we also allow the model coefficients to have different values in different regions of each horizontal plane using a selection based on the (resolved) coherent vortical structure. This is indicated by the superscript n for regions within which different physical processes occur. Equation (4.6) represents a new model which we denote the *dynamic anisotropic selective model* (DASM). The different spatial regions n in each horizontal plane are selected as follows:

(*a*) $n = a$, energy backscatter region. As shown in § 3.3, energy backscatter occurs at the splat region of hairpin vortex connection, where vortex surface-inclination angle α is large and horizontal divergence is positive. For our DASM implementation, we define region '*a*' as all points which satisfy $\alpha > 25^\circ$ and $\partial\bar{u}/\partial x + \partial\bar{v}/\partial y = -\partial\bar{w}/\partial z > 0$. Based on earlier discussions, we expect C_H^a to be negative near the free surface.

(*b*) $n = b$, small inter-scale energy transfer region. As discussed in § 3.3, in the region where coherent vorticity is connected to the free surface, the inter-scale energy transfer is expected to be weak and SGS dissipation is small or can be neglected. In our DASM, this region is defined by $\alpha < 5^\circ$ and $|\bar{\omega}_z| > 2\bar{\omega}_z^{rms}$, wherein we set $C_H^b = C_H^b = 0$.

(*c*) $n = c$, remaining region (without strong coherent vortical interactions). This is the 'typical' region and is expected to be dominated by forward energy transfer.

We point out that the 'selective' idea for the SGS modelling is not new. David (1993) developed a selective structure-function model based on the angle between the vorticity at a grid point and the vorticity averaged over the neighbouring points. When the angle is less than 20°, which means that the flow is not sufficiently three-dimensional, the SGS model is turned off to allow molecular dissipation only. The model is turn on only when the angle exceeds 20°. This selective structure-function model has been applied successfully to stratified flow over a backward-facing step (cf. Lesieur & Métais 1996).

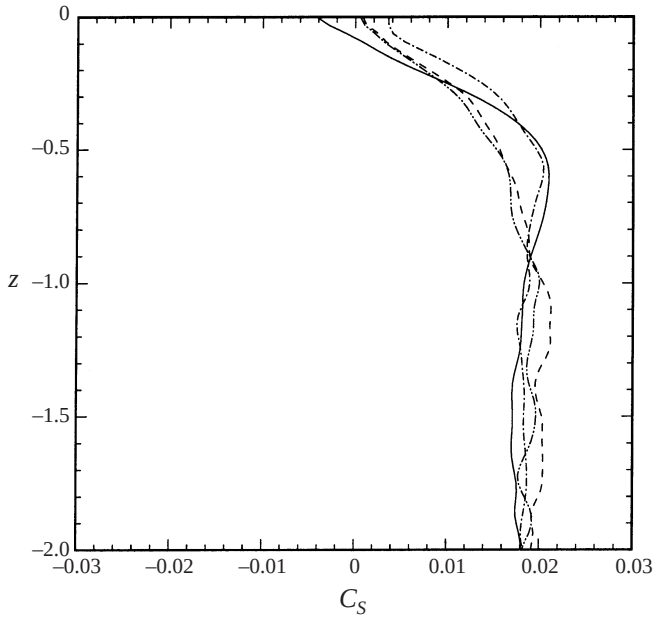

FIGURE 17. Vertical variations of DASM model coefficients: C_H^a (———), C_V^a (– – – –), C_H^c (– · – · –) and C_V^c (– · · – · · –) obtained from *a priori* test. $t = 60$.

We also remark that the DASM explicitly captures the anisotropic nature of free-surface turbulence; as a result, (4.6) satisfies rotational invariance only for the (vertical) z-axis. For large free-surface deformation (not considered here), (4.6) must at least be modified to refer to the local surface-normal/surface-parallel coordinates.

An indication of the efficacy of DASM over DSM is in *a priori* tests of the model against DNS data. Figure 16 also plots the correlation coefficient (3.18) between DASM and the SGS stress from DNS. Compared to DSM, DASM obtains better correlation, especially near the free surface. This suggests that the anisotropic and selective nature of DASM is more able to capture the processes near the free surface. This is confirmed in figure 17 which plots the vertical variations of the DASM model coefficients obtained from *a priori* test. In region a, it is seen that $C_H^a < 0$ as the free surface is approached, indicating energy backscatter. On the other hand, the difference between C_V^a and C_V^c is insignificant and both remain positive throughout the depth (but diminish towards the free surface).

Finally, we discuss the dynamic procedure for obtaining the DASM coefficients, $C_H^n(z,t)$, $C_V^n(z,t)$, $n = a, c$, in LES. At the coarse filter level, the SGS model is written as

$$T_{ij} - \tfrac{1}{3}\delta_{ij}T_{kk} = -2\hat{\bar{\Delta}}^2|\hat{\bar{S}}|\begin{pmatrix} C_H^n\hat{\bar{S}}_{11} & C_H^n\hat{\bar{S}}_{12} & C_V^n\hat{\bar{S}}_{13} \\ C_H^n\hat{\bar{S}}_{21} & C_H^n\hat{\bar{S}}_{22} & C_V^n\hat{\bar{S}}_{23} \\ C_V^n\hat{\bar{S}}_{31} & C_V^n\hat{\bar{S}}_{32} & C_H^n\hat{\bar{S}}_{33} \end{pmatrix}. \tag{4.7}$$

The Germano identity then gives

$$\mathscr{L}_{ij} - \tfrac{1}{3}\delta_{ij}\mathscr{L}_{kk} = \begin{pmatrix} C_H^n m_{11} & C_H^n m_{12} & C_V^n m_{13} \\ C_H^n m_{21} & C_H^n m_{22} & C_V^n m_{23} \\ C_V^n m_{31} & C_V^n m_{32} & C_H^n m_{33} \end{pmatrix}, \tag{4.8}$$

$\bar{\Delta}$	0.119	0.188	0.247	0.299	0.347	0.392
r	0.562	0.567	0.580	0.595	0.614	0.636

TABLE 1. Dependence of the DFFM model coefficient r on the LES filter width $\bar{\Delta}$.

where m_{ij} is as defined before. Finally, the DASM coefficients are solved by minimizing

$$\sum_{n=a,c}\sum_{ij=11,12,21,22,33}(\mathscr{L}_{ij}-\delta_{ij}\mathscr{L}_{kk}/3-C_H^n m_{ij})^2+\sum_{n=a,c}\sum_{ij=13,23,31,32}(\mathscr{L}_{ij}-C_V^n m_{ij})^2$$

on each horizontal plane. Note that the above procedure in effect neglects the variations of the model coefficients across boundaries between different regions but the net effect is found to be insignificant.

4.1.3. *Dynamic free-surface function model* (*DFFM*)

The results in § 3.2 (e.g. figure 6) show that, as a result of (reverse) energy cascade, the eddy viscosity exhibits a characteristic decrease in the free-surface boundary layer. It is, therefore, desirable if this variation and the structure of the free-surface boundary layer can be represented explictly in an SGS model. As discussed in § 3.4, the free-surface layer structure can be quantitatively defined in terms of the mean flow profile. Shen *et al.* (2000) found a similarity solution for the latter which is associated with a Gaussian profile for the turbulence diffusivity. These compared remarkably well with DNS. It is shown further in Shen *et al.* (2000) that, similar to the turbulence diffusivity, the Smagorinsky coefficient $C_S(z,t)$ near the free surface can also be described well by a Gaussian profile:

$$C_S(z,t)=C_{Sa}-(C_{Sa}-C_{S0})\exp[-z^2/(ra)^2]. \tag{4.9}$$

Here C_{Sa} is the value of the Smagorinsky coefficient in the bulk flow, C_{S0} its value at the free surface, and a is the thickness of the outer free-surface boundary layer defined to be the depth of the minimum of the mean flow profile. The coefficient r (found to be close to 0.6 in Shen *et al.* 2000) is a length-scale ratio to be specified.

We remark that (4.9) from Shen *et al.* (2000) is a result of the vanishing tangential stress boundary condition at the free surface. For problems where the tangential stress may be non-zero at the free surface, for example when wind stress or surfactants are present, Shen *et al.* (2000) and the Gaussian profile (4.9) need to be extended/modified.

We develop in this paper a dynamic free-surface function model (DFFM) based on (4.9) wherein the model coefficients C_{Sa}, C_{S0} and a are determined dynamically from the resolved flow. The coefficient r is not directly available from the resolved flow and may, in general, depend on the LES filter width $\bar{\Delta}$. Table 1 shows the variation of r as a function of $\bar{\Delta}$. The variation of r with $\bar{\Delta}$ is relatively small and justifies the use of a constant value of r in (4.9) which we set to be $r=0.6$ in our DFFM.

The dynamic scheme for the DFFM coefficients C_{Sa} and C_{S0} is derived from the model SGS equations for two filter levels $\overline{G}$ and $\hat{\overline{G}}$:

$$\tau_{ij}-\tfrac{1}{3}\delta_{ij}\tau_{kk}=-2\{C_{Sa}-(C_{Sa}-C_{S0})\exp[-z^2/(ra)^2]\}\bar{\Delta}^2|\bar{s}|^2\bar{s}_{ij}, \tag{4.10}$$

and

$$T_{ij}-\tfrac{1}{3}\delta_{ij}T_{kk}=-2\{C_{Sa}-(C_{Sa}-C_{S0})\exp[-z^2/(ra)^2]\}\hat{\bar{\Delta}}^2|\hat{\bar{s}}|^2\hat{\bar{s}}_{ij}. \tag{4.11}$$

Using the Germano identity, we obtain

$$\mathscr{L}_{ij} - \tfrac{1}{3}\delta_{ij}\mathscr{L}_{kk} = \{C_{Sa} - (C_{Sa} - C_{S0})\exp[-z^2/(ra)^2]\}m_{ij}, \tag{4.12}$$

where m_{ij} is defined as before. Instead of averaging over each horizontal plane, the coefficients C_{Sa} and C_{S0} are determined by best matching (4.12) over the entire fluid volume. Least-square minimization then gives

$$\int_{-D}^{0} \mathscr{W}(z)\langle(\mathscr{L}_{ij} - \tfrac{1}{3}\delta_{ij}\mathscr{L}_{kk} - C_{Sa}\{1 - \exp[-z^2/(ra)^2]\}m_{ij} - C_{S0}\exp[-z^2/(ra)^2]m_{ij})^2\rangle \mathrm{d}z.$$

In the above, $\mathscr{W}(z)$ is a weighting function which we choose to be $\mathscr{W}(z) = \exp[-z^2/(2ra)^2]$ to place more weight on the near-free-surface region.

Finally, the outer layer thickness $a(t)$ is determined from the resolved mean shear profile by the location where the (local) minimum (first) occurs in the near-surface region.

4.2. *Evaluation of SGS models for free-surface flux and dynamic pressure*

Before we consider the performance of the SGS stress models in § 4.1 in (*a posteriori*) LES, we first evaluate the models for the SGS free-surface flux and dynamic pressure discussed in § 2.2.

In this study, the benchmark data are obtained from DNS of the free-surface shear flow on a fine 128^2(horizontally) $\times$ 192 (vertically) grid with timestep 0.005. To obtain smooth statistics, a set of 25 DNS datasets (with different initial seeds) is obtained. For LES we use a coarse $32^2 \times 96$ grid with timestep 0.02. We start the LES with the filtered DNS field at $t = 60$, and run the simulation for 10 time units, which is sufficient for the free-surface turbulence features (e.g. the surface-connecting vortices) to evolve significantly. A total of 25 LES runs corresponding to the DNS are also performed. The LES results are then compared with the filtered DNS data at $t = 70$.

The grid filter $\overline{G}$ is introduced in § 3. The test filter $\widehat{G}$ is similar to $\overline{G}$ and uses Gaussian filters in the (periodic) horizontal directions but no filtering in the vertical direction is now applied. The filter width for $\widehat{G}$ is chosen to satisfy $\hat{\bar{\Delta}}_x = 2\bar{\Delta}_x$ and $\hat{\bar{\Delta}}_y = 2\bar{\Delta}_y$. The overall filter width at the coarse level, $\hat{\overline{G}}$, is defined as

$$\hat{\bar{\Delta}} \equiv (\hat{\bar{\Delta}}_x \hat{\bar{\Delta}}_y \bar{\Delta}_z)^{1/3} = 0.4749. \tag{4.13}$$

Figure 18 shows the *a priori* performances of the scale-similar SGS model (2.31) for the free-surface flux, and the Yoshizawa SGS model (2.20) for the free-surface dynamic pressure p_{SGS} in (2.19). The overall performance in terms of the correlation

$$\mathrm{Cor}\langle\tau, M\rangle \equiv \frac{\langle(\tau - \langle\tau\rangle)(M - \langle M\rangle)\rangle}{(\tau - \langle\tau\rangle)^{rms}(M - \langle M\rangle)^{rms}}. \tag{4.14}$$

is excellent ($\sim$ 0.9) for the SGS flux, and acceptable ($\sim$ 0.7) for the free-surface dynamic pressure. (Note that the mean value is subtracted from (4.14). If the mean value is not subtracted, the correlation coefficient for the p_{SGS} is close to 0.8.)

The efficacy of the modelling of the SGS free-surface terms τ_u^{kbc}, τ_v^{kbc} and p_{SGS} is demonstrated in *a posteriori* tests. Figure 19 compares the free-surface elevation and horizontal surface vorticity $\omega_s \equiv (\omega_x^2 + \omega_y^2)^{1/2}|_{z=0}$ between the LES and DNS results. For LES without SGS, the results depart from the DNS values and grow in time in a non-physical manner. Comparing the LES results (with DSM for the SGS stress) with and without SGS models for $\tau_{u,v}^{kbc}$ and p_{SGS}, the improvement with the latter

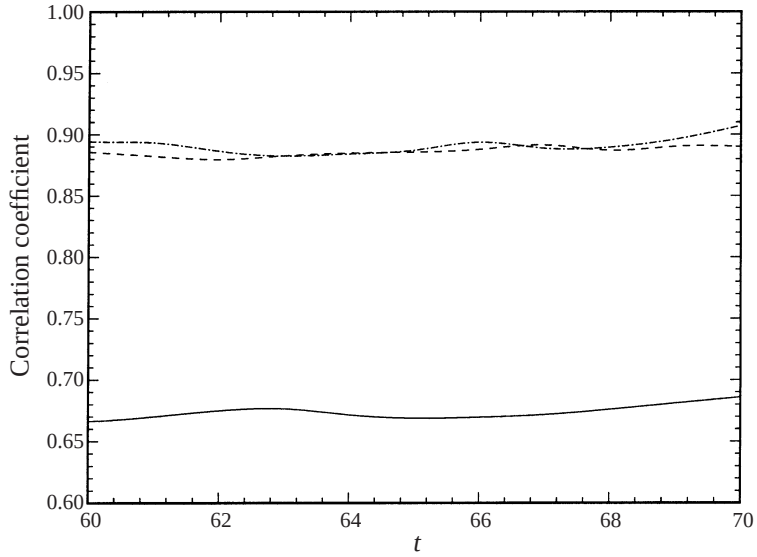

FIGURE 18. Correlation coefficients from *a priori* tests of SGS models for free-surface dynamic pressure p_{SGS} (———), and free-surface flux terms: τ_u^{kbc} (– – – –) and τ_v^{kbc} (–·–·–).

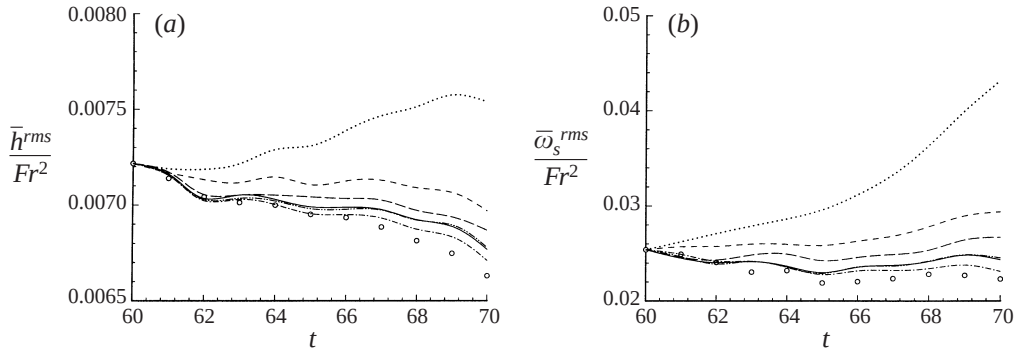

FIGURE 19. Time evolutions of (*a*) the free-surface elevation $\bar{h}^{rms}/Fr^2$, and (*b*) the horizontal surface-vorticity magnitude $\bar{\omega}_s^{rms}/Fr^2$ obtained using: ○, DNS; ·····, simulation on coarse grid without any model; – – – –, DSM without SGS models for free-surface flux and dynamic pressure; and with SGS models for free-surface flux and dynamic pressure: ———, DSM; –·–·–, DFFM; and –··–··–, DASM. The curve —— —— represents DSM with the scale-similarity model (4.15) instead of the Yoshizawa expression (2.20) for p_{SGS}.

is quite appreciable. Of the two, our results (not shown in figure 19) show that the modelling of p_{SGS} accounts for about 70% of the total observed improvement.

We remark that in addition to the Yoshizawa expression (2.20), we have also tested a dynamic scale-similarity model for the SGS contribution to the dynamic pressure:

$$p_{SGS} \equiv \frac{\overline{u_k u_k} - \bar{u}_k \bar{u}_k}{3} = C_{p,B} \frac{\overline{\bar{u}_k \bar{u}_k} - \bar{\bar{u}}_k \bar{\bar{u}}_k}{3}. \tag{4.15}$$

Although this model obtains a high correlation coefficient (~ 0.9) in the *a priori* test, our *a posteriori* test shows that it does not provide surface statistics as satisfying as the Yoshizawa model (figure 19).

Figure 20 plots the dynamic model coefficient values for C_{kbc} in (2.31) and C_p in

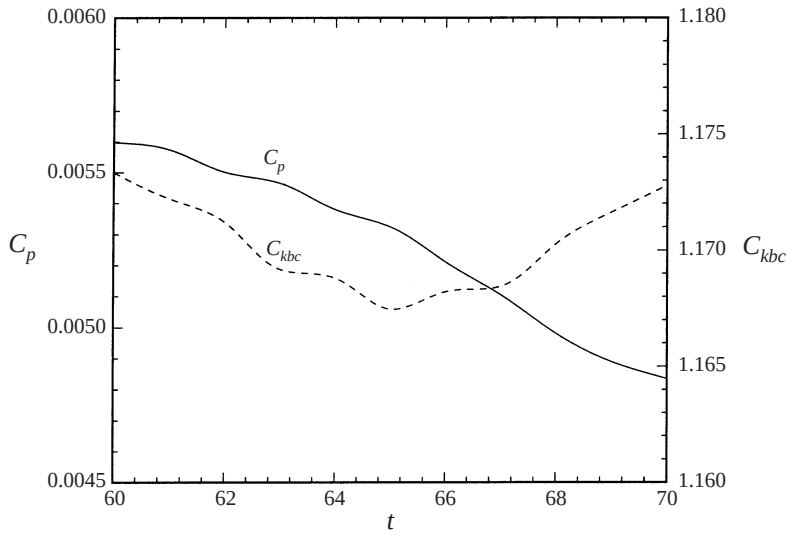

FIGURE 20. Time variations of the coefficients of the SGS models for the free-surface pressure p_{SGS}, C_p (———); and free-surface flux $\tau_{u,v}^{kbc}$, C_{kbc} (– – – –).

(2.20) obtained in the DSM results of figure 19. The coefficient C_{kbc} for the scale-similarity model has the value around 1.17 which is close to the coefficient value of the scale-similarity model for the SGS stress (see figure 34). The coefficient C_p in the Yoshizawa expression varies from 0.0056 to 0.0047, which is larger than the Smagorinsky coefficient near the free surface (cf. figure 21).

For non-vanishing Froude numbers, it is clear that the modelling of the free-surface SGS terms p_{SGS} and $\tau_{u,v}^{kbc}$ is essential. In all subsequent LES results, the SGS models for these terms (2.20) and (2.31) are always used. We note that the need for SGS modelling in the kinematic boundary condition was also pointed out (but not implemented) by Hodges & Street (1999). The modelling of the SGS contribution to the dynamic pressure at the free surface appears to be new in the present context.

4.3. *Evaluation of SGS stress models for free-surface turbulence*

The SGS stress models introduced in § 4.1, DSM, DFFM and DASM, are tested in (*a posteriori*) LES simulations against DNS results. We examine in order: the variation of the model coefficients, predictions of turbulence intensity, mean flow and free-surface vortical statistics.

4.3.1. *Model coefficients*

In § 3, we observed that the magnitude of the energy cascade from the resolved scales to the subgrid scales decreases significantly as the free surface is approached. Consequently, the Smagorinsky coefficient C_S should also decrease towards the surface (figure 6). Figure 21 compares the model coefficients of DSM and DFFM against DNS-fitted values. Both models capture the decreasing trend of C_S towards the surface, but when a more physically based form of the profile is used in DFFM, the comparison is appreciably improved in both the vertical extent and quantitative value.

Turning to DASM, the dynamic scheme provides, at each time, separate profiles for C_H^n, C_V^n for each region $n = a, c$ (we set $C_{H,V}^b \equiv 0$). The results are plotted in figure 22. Comparing these to DNS-fitted curves in figure 17, it is seen that the dynamic and DNS (*a priori*) values compare almost perfectly. The depths over which C_H and C_V

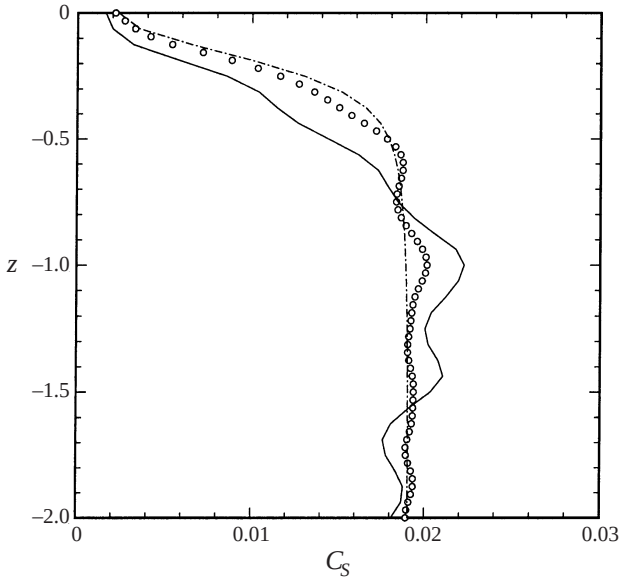

FIGURE 21. Profile of the model coefficient C_S from: ○, DNS; ———, DSM; and –·–·–, DFFM. The profiles are averaged from $t = 60$ to $t = 70$.

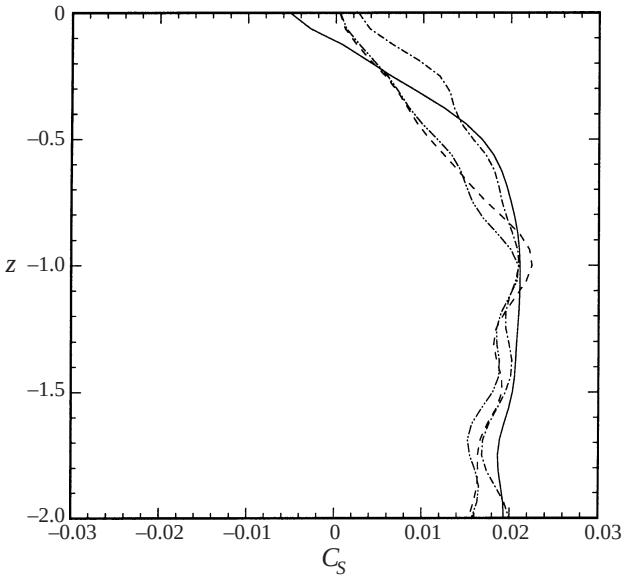

FIGURE 22. Profiles of the model coefficient in DASM: ———, C_H^a; – – – –, C_V^a; –·–·–, C_H^c; and –··–··–, C_V^c. The profiles are averaged from $t = 60$ to $t = 70$.

vary are different: C_V^n are very close for $n = a, c$, while C_H^a and C_H^b differ qualitatively near the free surface.

4.3.2. *Turbulence intensity*

Figure 23 compares the DNS and LES predictions of the turbulent kinetic energy of grid-scale motions, $\bar{q}^2/2 \equiv \langle(\bar{u}_i - \langle\bar{u}_i\rangle)^2\rangle/2$. In the absence of any SGS model, $\bar{q}^2$ is

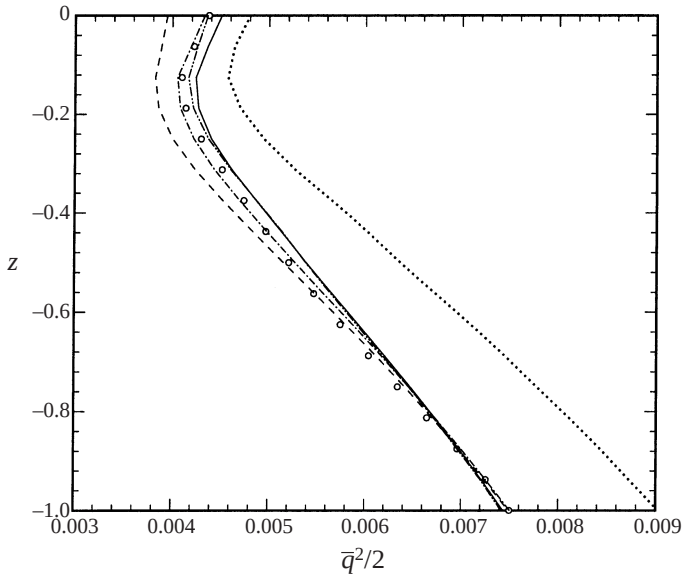

FIGURE 23. Grid-scale turbulent kinetic energy $\bar{q}^2/2$ obtained from: o, DNS; ·····, simulation on coarse grid without any model; and LES using: – – – –, CSM; ———, DSM; –·–·–, DFFM; –··–··–, DASM. $t = 70$.

over-predicted at all depths as expected. In addition to DSM, DASM and DFFM, we plot for comparison the results using a constant Smagorinsky model (CSM) where a single constant value of C_S, set equal to the time-averaged bulk value obtained in DSM, is used for the LES. CSM, which does not capture the decrease in eddy viscosity at the surface, results in a $\bar{q}^2$ which is over-dissipated there. Indeed the error in CSM at the surface is comparable in magnitude (but with opposite sign) to that when no SGS model is used.

When vertical variation in the model coefficient is allowed, DSM obtains a reasonable kinetic energy profile, although since DSM slightly under-predicts C_S at the surface (figure 21), the corresponding prediction of $\bar{q}^2$ there is somewhat high. The new SGS models, DFFM and DASM, capture the variation of the model coefficients over the surface layer more precisely and obtain more accurate $\bar{q}^2$ predictions near the free surface. Of the two, DFFM, which captures more physically the near-surface turbulence diffusion mechanism (Shen *et al.* 2000), delivers a slightly better overall $\bar{q}^2$ prediction.

Figure 24 presents similar results for the components of $\bar{q}^2$ which reveals the anisotropy of the flow. Without the SGS model, all components are substantially over-predicted. CSM under-predicts all the components but especially the horizontal ones relative to the other dynamic models. DSM is able to capture the anisotropy although the horizontal fluctuations are higher than the benchmark data because of the underestimation of C_S. With DFFM and DASM, improvements over DSM can be seen.

4.3.3. *Mean flow*

We compare the LES predicted mean velocity profiles in figure 25. Although there is improvement over the no SGS model case, CSM, DSM, DFFM and DASM are all not satisfactory relative to their predictions of the kinetic energy. The reason is that,

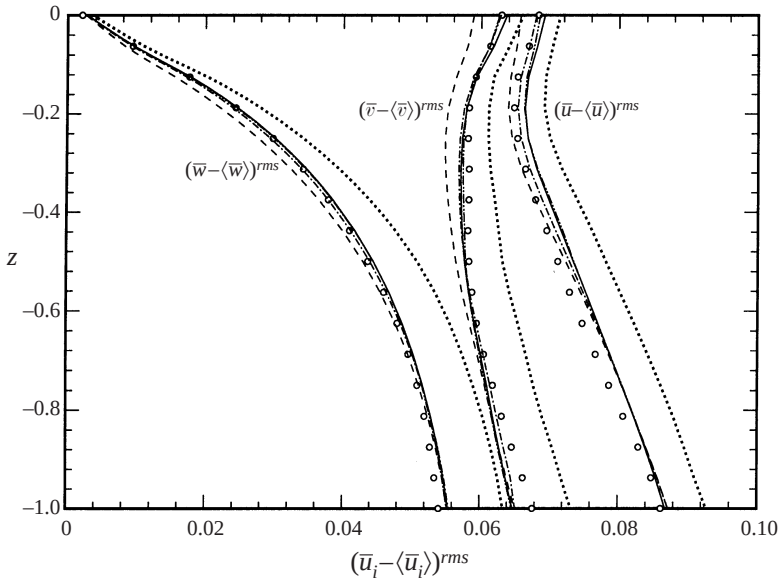

FIGURE 24. Profiles of the grid-scale velocity fluctuation components $(\bar{u}_i-\langle\bar{u}_i\rangle)^{rms}$, $i = 1, 2, 3$, obtained from: ○, DNS; ·····, no SGS model; – – – –, CSM; ———, DSM; –·–·–, DFFM; –··–··–, DASM. $t = 70$.

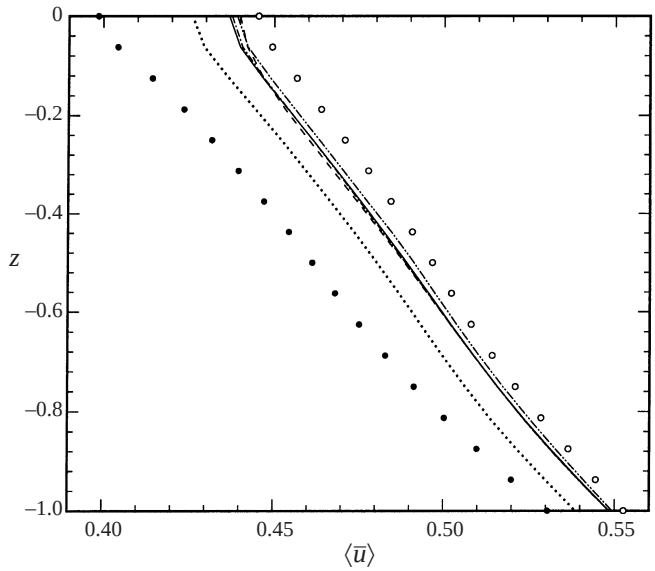

FIGURE 25. The mean velocity profile $\langle\bar{u}\rangle$ at $t = 70$: ○, DNS; ·····, no SGS model; – – – –, CSM; ———, DSM; –·–·–, DFFM; –··–··–, DASM; ●, the initial LES profile from DNS at $t = 60$.

while eddy-viscosity models obtain the correct overall SGS dissipation, the correlation between the predicted and actual SGS stress itself is poor (cf. figure 16). As will be shown in § 4.4, a combination of such models with a scale-similarity (Bardina-type) model improves the mean velocity predictions significantly.

The most significant gain in using a surface-function-type model like DFFM is in the prediction of the mean shear profile $\langle\bar{u}_z\rangle(z)$ (figure 26). The mean shear

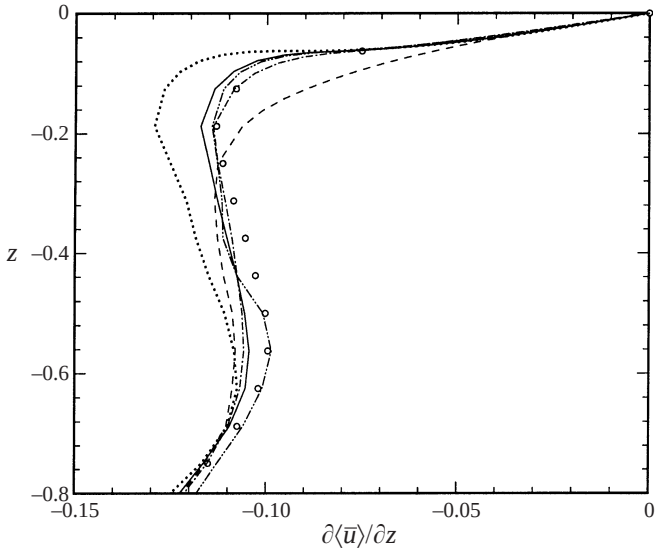

FIGURE 26. Mean shear profile $\partial\langle\bar{u}\rangle/\partial z$ obtained from: ○, DNS; ·····, no SGS model; – – – –, CSM; ———, DSM; – · – · –, DFFM; – ··· – ···–, DASM. $t = 70$.

profile quantitatively defines the surface layer structure in that, as the free surface is approached, its magnitude initially increases over the outer boundary layer, reaches a maximum and then drops to zero inside a much thinner inner layer (cf. Shen *et al.* 2000). Figure 26 shows that CSM has a large error comparable to the no-model case, and in particlar predicts a much thicker surface layer. DSM and DASM, which obtain the decreasing trend in the eddy viscosity, capture the surface layer reasonably well. Since the physical functional behaviour of the surface layer is represented in DFFM, it predicts $\langle\bar{u}_z\rangle(z)$ with remarkable accuracy.

4.3.4. *Free-surface vortical statistics*

LES predictions of the free-surface roughness $\bar{h}^{\rm rms}$ and horizontal surface vorticity $\bar{\omega}_s^{\rm rms}$ are shown in figure 19. As pointed out there, proper SGS modelling of free-surface flux and dynamic pressure is essential. With these models, DSM, DASM and DFFM all perform adequately for such averaged statistics.

The observable turbulence features on the surface are of immediate importance to applications. These features are dominated by near-surface vortical mechanisms such as surface connection which result in persistent and prominent surface signatures. Because of the uncertainty in the subgrid-scale motions (cf. Lesieur & Métais 1996), it is inappropriate to compare the evolution of a specific vortical structure in the LES. We resort instead to statistical measures of the structure of the coherent surface vorticity.

Figure 27 plots the time evolution of the area percentage of coherent surface-connected vortices, $\mathscr{A}_b$, which we define as the percent of surface area satisfying $|\bar{\omega}_z| > 2\bar{\omega}_z^{rms} \cup \alpha < 5^\circ$. Note that this is the same as region $n = b$ of DASM. Because of the persistence of such vorticity, $\mathscr{A}_b$ generally increases with time, as shown by the DNS data. DSM, which does not account for either energy backscatter during the vortex connection or reduced dissipation of surface-connected vortices, tends to over-dissipate the surface vortices and hence under-predicts $\mathscr{A}_b$. Since DFFM also uses a single model coefficient in the horizontal plane, the improvement of DFFM

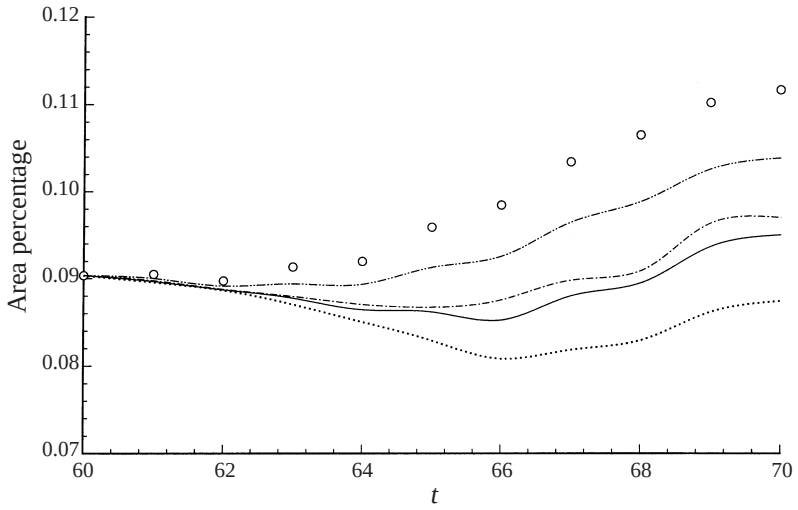

FIGURE 27. Time evolution of the area percentage of coherent surface-connected vortices $\mathscr{A}_b$ for: ○, DNS; ·····, no SGS model; ———, DSM; –·–·–, DFFM; –··–··–, DASM.

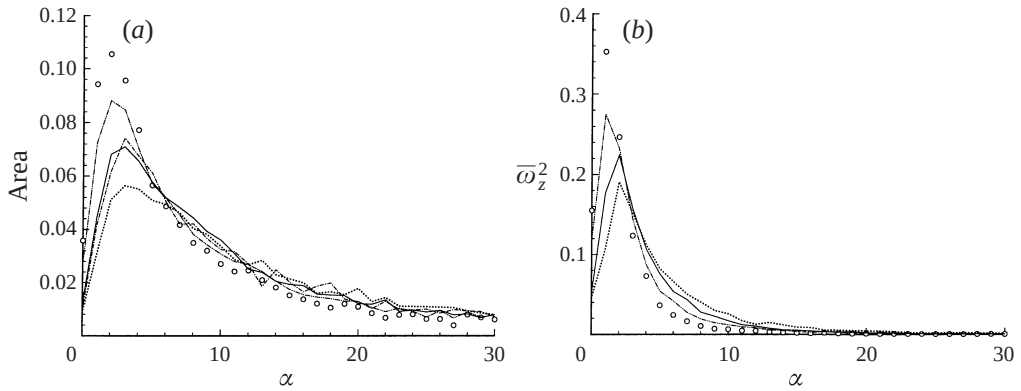

FIGURE 28. Distributions of (*a*) $\mathscr{A}(\alpha)$; and (*b*) $\bar{\omega}_z^2(\alpha)$ as functions of the vorticity surface-inclination angle α obtained with: ○, DNS; ·····, no SGS model; ———, DSM; –·–·–, DFFM; –··–··–, DASM.

over DSM is small. On the other hand, since DASM uses a selective procedure based on the resolved vorticity structure information, it obtains a significantly better prediction for $\mathscr{A}_b$.

As discussed in § 3.3, the surface-inclination angle α is an important measure of the evolution of surface-connecting vortices. To further elucidate the efficacy of the LES schemes for predicting surface signatures, we examine the distribution of percentage surface area $\mathscr{A}$ and surface enstrophy $\bar{\omega}_z^2$ as a function of the grid-scale inclination angle α. These are plotted in figure 28. The dominance of surface-connected vorticity (low α) is evident. Compared to DNS data, DSM and DFFM both tend to under-predict the low-α values as a result of over-dissipation of connection events (with a single C_S in the horizontal plane). DASM continues to perform well here although the peaks in $\mathscr{A}(\alpha)$ and $\bar{\omega}_z^2(\alpha)$ are under-predicted since the number of selection regions n used is still relatively small.

The superiority of DASM for surface signatures is further seen in the conditionally

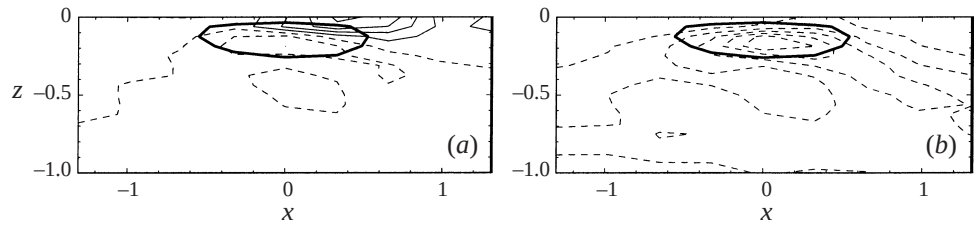

FIGURE 29. Contours of VISA SGS dissipation rate $\tau_{ij}\bar{s}_{ij}$ around hairpin vortices, with the head portion located at $(0, 0, -0.0625)$. Results obtained with: (*a*) DASM (contour interval 0.0002); and (*b*) DSM (contour interval 0.00002). Dashed lines represent negative values. The thick line is the contour $\omega_y = -0.5$, which marks the location of the hairpin head.

averaged flow field around LES-resolved coherent hairpin vortices. Figure 29 plots the VISA SGS dissipation rate around connecting hairpin vortices. Because of the negative values of C_H^a (figure 22), DASM captures energy backscatter at the splat region of the hairpin vortex. This is in agreement with the *a priori* results in § 3.3. In comparison, DSM, which uses a single model coefficient in the plane, does not capture the inverse energy transfer. Thus, although the plane-averaged value is correct in DSM, the local SGS dissipation rate around this event is off in both sign and magnitude.

4.4. *SGS models tested at higher Reynolds and Froude numbers*

The proceeding evaluations of SGS models are tested against our DNS dataset for a free-surface turbulent shear flow at fixed (and relatively low) Reynolds number ($Re = 1400$) and Froude number ($Fr = 0.7$). To further validate the new SGS models, we apply our models to a flow with higher Reynolds ($Re = 3000$) and Froude ($Fr = 1.4$) numbers. The benchmark data are obtained from direct numerical simulations at a very fine mesh with $256 \times 256 \times 384$ grids (the DNS of the preceding lower Reynolds and Froude number case uses a $128 \times 128 \times 192$ grid). For the LES, we use the same coarse $32 \times 32 \times 96$ grid.

Figure 30(*a*) compares the turbulent kinetic energy profiles. For this higher Reynolds and Froude number case, the improvement of the new DFFM and DASM over the existing DSM is much better than that obtained in figure 23. This is also true for the mean shear profiles shown in figure 30(*b*). At these higher Reynolds and Froude numbers, the performance of the DSM is even worse (figure 30*a*, *b*) than before. In this case, the DFFM is found to capture accurately the variation of turbulence statistics near the free surface. The DASM results, although not as good as those of the DFFM, are still superior to the DSM.

Figure 31 compares the statistics of the free-surface coherent structures. Consistent with the preceeding results (figures 27 and 28) and more clearly so, the DASM is found to capture the surface coherent signature statistics very accurately. The DFFM also performs well, while the DSM is not satisfactory for this higher Reynolds and Froude number case.

In summary, while the DFFM and DASM are established using DNS results at a lower Reynolds/Froude number, their performance for a higher Reynolds/Froude number case remains satisfactory. On the other hand, the DSM, which was inferior to the DFFM and DASM, performs even more poorly here. This is a further validation of the new DFFM and DASM. The improved relative performance of the new models is mainly due to the fact that for the higher Reynolds number, the magnitude of the

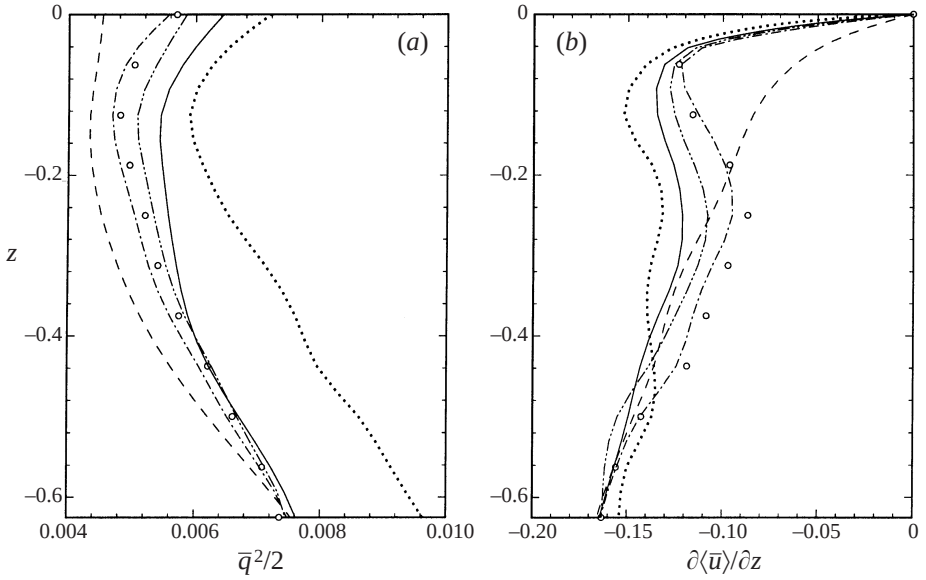

FIGURE 30. Profiles of (*a*) grid-scale turbulent kinetic energy $\bar{q}^2/2$, and (*b*) mean shear $\partial\langle\bar{u}\rangle/\partial z$ obtained from: ○, DNS; ·····, simulation on coarse grid without any model; and LES using: – – – –, CSM; ———, DSM; – · – · –, DFFM; – ·· – ·· –, DASM. $Re = 3000$ and $Fr = 1.4$.

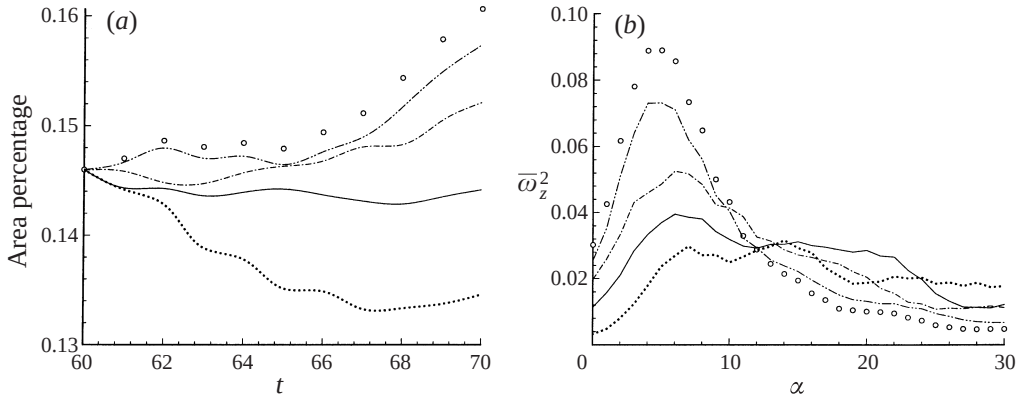

FIGURE 31. (*a*) Time evolution of the area percentage of coherent surface-connected vortices $\mathscr{A}_b$, and (*b*) distributions of $\bar{\omega}_z^2(\alpha)$ as functions of the vorticity surface-inclination angle α. ○, DNS; ·····, no SGS model; ———, DSM; – · – · –, DFFM; – ·· – ·· –, DASM. $Re = 3000$ and $Fr = 1.4$.

viscous terms becomes smaller, and proper SGS modelling becomes more important. It would be interesting to see how the DFFM and DASM would perform at even higher Reynolds numbers. Unfortunately, we are already near the limit of available computational capacity. For substantially higher *Re*, experimental benchmark data would be invaluable.

4.5. *Discussion*

In this study, we have developed two new SGS stress models, DFFM and DASM, for free-surface turbulent flows. Table 2 summarizes the performance of the new models relative to the existing CSM and DSM. Also given in table 2 are the relative

	CSM	DSM	DFFM	DASM
Related physics of free-surface turbulence			multi-level surface-layer structure	anisotropy and energy backscatter
Model coefficient	C	$C(z)$	C_{Sa} and C_{s0}	$C_H^n(z)$ and $C_V^n(z)$
Performance for turbulence intensity	poor	average	excellent	good
Performance for mean shear	poor	average	excellent	good
Performance for surface signatures		average	good	excellent
CPU time per timestep (seconds)	1.28	2.12	2.79	2.75

TABLE 2. Key features of the SGS stress models CSM, DSM, DFFM and DASM. CPU time is measured for runs with a $32 \times 32 \times 96$ grid on DEC AlphaStation 500/500.

computational costs. Overall, the new DFFM and DASM are superior to the existing models for free-surface turbulence.

For free-surface turbulence, the SGS stress model results show that it is important for eddy-viscosity models to capture the spatial variations of model coefficients both vertically and horizontally: vertically because of the decrease in eddy viscosity over the surface layer due to energy backscatter; and horizontally because of its disparate behaviour associated with large-scale vortical events.

Dynamic procedures in the vertical direction in DSM and DASM have a substantial advantage over CSM in obtaining the vertical variations, but a model that incorporates known physical structure(s) such as DFFM captures the surface layer with remarkable accuracy. When model coefficients in the horizontal plane are allowed to take on different values in a selective scheme, as in DASM (based on coherent vorticity dynamics and reflected differently in different directional components), the prediction of the statistics of coherent events is greatly improved. One may suggest that a point-by-point dynamic scheme would do even better. However, such procedures, without some *ad hoc* averaging, are prone to instability (when the model coefficient varies excessively) (cf. Germano *et al.* 1991). Advanced localization formulations (e.g. Ghosal *et al.* 1995) either constrain the occurrence of negative eddy viscosity, which does not allow energy backscatter, or introduce additional transport equations, which substantially increase the degree of complexity. Additional research in these areas is needed.

While eddy-viscosity models do an excellent job in modelling the total dissipation, they can be inadequate in certain aspects, for example in predicting the mean profile here. In this case, the correlation between the modelled and actual SGS stress is poor, because their principal axes are not generally aligned. As the free surface is approached, the correlation becomes even worse. To overcome this drawback, a powerful idea is to combine the eddy-viscosity model with a scale-similarity model (cf. Bardina *et al.* 1983; and e.g. Zang, Street & Koseff 1993; Salvetti *et al.* 1997). This is pursued in the next section.

4.6. *Combination of eddy-viscosity and scale-similarity models*

Each of the SGS models in § 4.1 can be used in combination with a dynamic scale-similarity model. In this case, the DSM, DFFM and DASM approaches become

respectively:

$$\tau_{ij} - \tfrac{1}{3}\delta_{ij}\tau_{kk} = -2C_S\bar{\Delta}^2|\bar{s}|^2\bar{s}_{ij} + C_B(L^m_{ij} - \tfrac{1}{3}\delta_{ij}L^m_{kk}), \tag{4.16}$$

$$\tau_{ij} - \tfrac{1}{3}\delta_{ij}\tau_{kk} = -2\{C_{Sa} - (C_{Sa} - C_{S0})\exp[-z^2/(ra)^2]\}\bar{\Delta}^2|\bar{s}|^2\bar{s}_{ij} + C_B(L^m_{ij} - \tfrac{1}{3}\delta_{ij}L^m_{kk}), \tag{4.17}$$

and

$$\tau_{ij} - \tfrac{1}{3}\delta_{ij}\tau_{kk} = -2\bar{\Delta}^2|\bar{s}| \begin{pmatrix} C^n_H\bar{s}_{11} & C^n_H\bar{s}_{12} & C^n_V\bar{s}_{13} \\ C^n_H\bar{s}_{21} & C^n_H\bar{s}_{22} & C^n_V\bar{s}_{23} \\ C^n_V\bar{s}_{31} & C^n_V\bar{s}_{32} & C^n_H\bar{s}_{33} \end{pmatrix} + C_B(L^m_{ij} - \tfrac{1}{3}\delta_{ij}L^m_{kk}). \tag{4.18}$$

These we denote by DSM+B, DFFM+B and DASM+B respectively. In the above, $L^m_{ij} \equiv \overline{\bar{u}_i\bar{u}_j} - \bar{\bar{u}}_i\bar{\bar{u}}_j$, and C_B is the coefficient of the scale-similarity model to be determined dynamically. Note that the combined model DSM+B (4.16) is identical to the dynamic two-parameter model (DTM) in Salvetti & Banerjee (1995) and Salvetti *et al.* (1997).

To determine the model coefficients, a similar dynamic procedure as before is applied. By using filters at two different levels and employing the Germano identity, we obtain respectively

$$\mathscr{L}_{ij} - \tfrac{1}{3}\delta_{ij}\mathscr{L}_{kk} = C_S m_{ij} + C_B H_{ij}, \tag{4.19}$$

$$\mathscr{L}_{ij} - \tfrac{1}{3}\delta_{ij}\mathscr{L}_{kk} = \{C_{Sa} - (C_{Sa} - C_{S0})\exp[-z^2/(ra)^2]\}m_{ij} + C_B H_{ij}, \tag{4.20}$$

and

$$\mathscr{L}_{ij} - \tfrac{1}{3}\delta_{ij}\mathscr{L}_{kk} = \begin{pmatrix} C^n_H m_{11} & C^n_H m_{12} & C^n_V m_{13} \\ C^n_H m_{21} & C^n_H m_{22} & C^n_V m_{23} \\ C^n_V m_{31} & C^n_V m_{32} & C^n_H m_{33} \end{pmatrix} + C_B H_{ij}. \tag{4.21}$$

Here $\mathscr{L}_{ij}$ and m_{ij} have the same definitions as before, while $H_{ij} \equiv \widehat{\bar{\bar{u}}_i\bar{\bar{u}}_j} - \hat{\bar{\bar{u}}}_i\hat{\bar{\bar{u}}}_j$. Finally, the coefficients are solved by least-squares matching of (4.19), (4.20) and (4.21) respectively. The correlation coefficients between the actual SGS stress and those predicted by DSM+B and DASM+B have been plotted in figure 16. As expected based on previous studies, the correlation is improved significantly at all depths when the scale-similarity model is added. In particular, the predictions of the combined models show no degradation in the surface layer in contrast to the Smagorinsky model alone.

The three combined models, DSM+B, DFFM+B and DASM+B, have been implemented and studied extensively in *a posteriori* LES tests. Overall, we obtain noticeable but not substantial improvements in the results for turbulent kinetic energy and free-surface statistics in § 4.2 and § 4.3. The most marked improvement of the combined models is in the prediction of the mean flow profile, which we focus on. Figure 32 compares the performance of the three SGS schemes with and without the scale-similarity model. Relative to the results without SGS models, the improvement of the combined models over the eddy-viscosity models alone is quite substantial.

Finally, we plot the dynamic model coefficients for DSM+B, DFFM+B and DASM+B. Figure 33 shows that the coefficients of the eddy-viscosity portion of the models preserve the same qualitative trends as those in § 4.3. The magnitudes of the coefficients of the combined models are, however, reduced significantly. This can be explained by the fact that less burden is put on the eddy-viscosity portion of the models to capture the SGS stress, a feature in favour of numerical stability (Zang *et al.* 1993; Salvetti *et al.* 1997). Figure 34 plots the profiles of C_B for DSM+B and DASM+B.

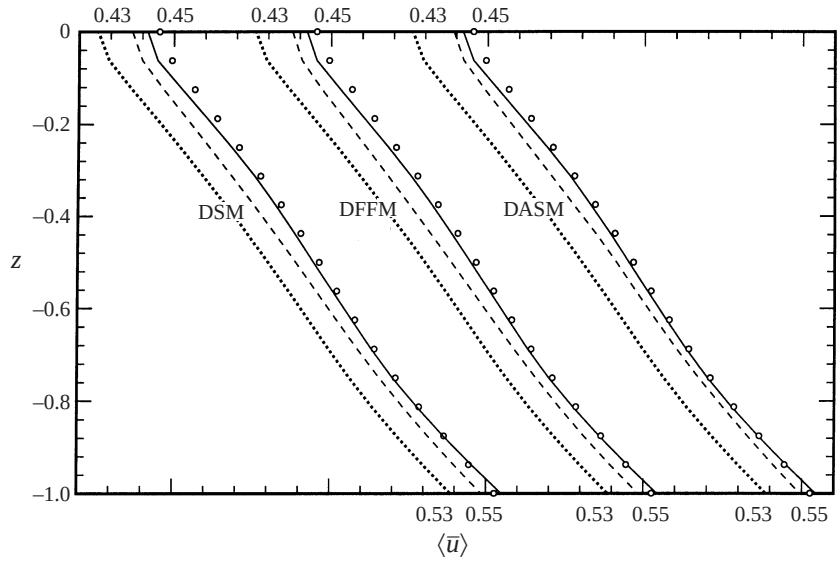

FIGURE 32. Mean velocity profile $\langle \bar{u} \rangle$ obtained using: DNS (○), simulation on coarse grid without any model (·····), and eddy-viscosity models with (———) and without (– – – –) scale-similarity model for DSM, DFFM and DASM. $t = 70$.

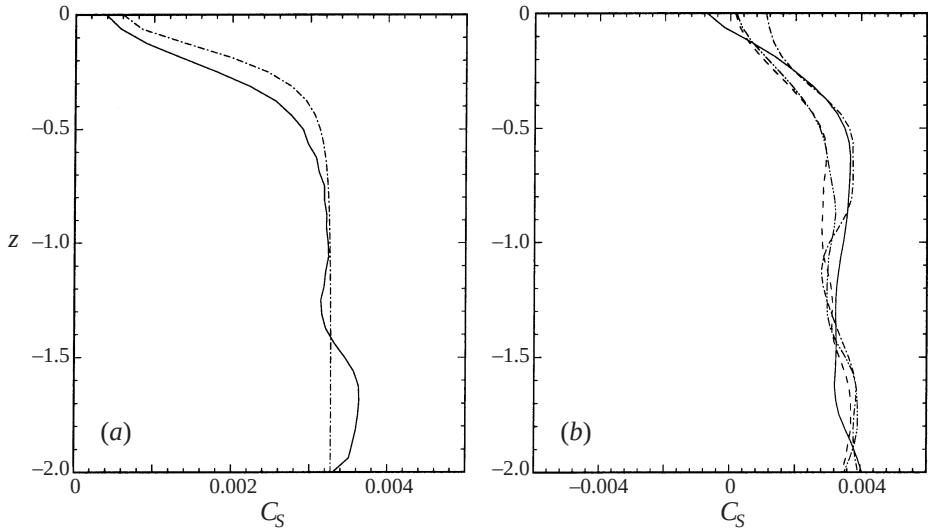

FIGURE 33. Profiles of eddy-viscosity model coefficients for: (*a*) ———, DSM+B; and –·–·–, DFFM+B; and (*b*) DASM+B for ———, C_H^a; – – – –, C_V^a; –·–·–, C_H^c; –··–··–, C_V^c. The profiles are averaged from $t = 60$ to $t = 70$.

The variations of C_B within the surface layer is small and may justify the use of a single value of C_B for all the depths. This affords a simplification for DFFM+B where all the model coefficients are determined by least-squares minimization over the whole volume.

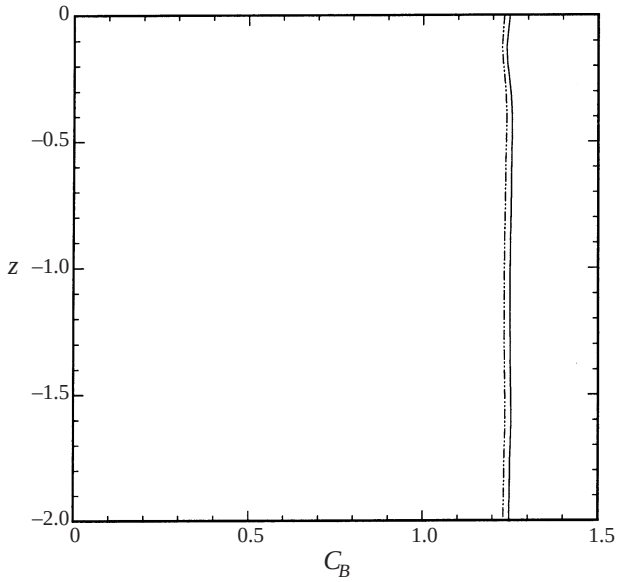

FIGURE 34. Profiles of the coefficient of the scale-similarity model C_B for: ———, DSM+B; and –··–··–, DASM+B.

5. Conclusions

In this study we investigate the large-eddy simulation of free-surface turbulent flows. The canonical problem we study is a turbulent shear flow beneath a free surface at small finite Froude numbers. The benchmark data are obtained from DNS on a fine grid. We first investigate the physics of the flow using an ensemble of DNS data which show the following: (i) The energy cascade from grid scales to subgrid scales decreases significantly at the free surface. (ii) The inter-scale energy transfer is strongly correlated with the coherent free-surface vortical structures; in particular, energy backscatter occurs at the splat region during the connection of a hairpin vortex to the free surface. (iii) The SGS stress components are highly anisotropic. At the splat region, only the horizontal components of the SGS stress react to the energy backscatter.

Based on this understanding, we develop LES with specialized SGS models for free-surface turbulence. These include SGS models for free-surface fluxes which come from the kinematic free-surface boundary condition, and for a dynamic SGS pressure which results from the imposition of a boundary condition on the total pressure at the free surface. These are obtained in the present context for the first time. For the SGS stress, we employ an existing dynamic Smagorinsky model (DSM), and develop two new models: a dynamic free-surface function model (DFFM) which captures the expected depth variation in the eddy viscosity (based on the similarity solution of Shen *et al.* 2000); and a dynamic anisotropic selective model (DASM), which recognizes the anisotropy of the flow field and the different energy cascade mechanisms which are coupled with the coherent surface vorticity dynamics.

Our numerical tests show that modelling of the free-surface SGS fluxes and dynamic pressure is important for the LES, especially in predicting the surface roughness. Compared with DSM, DFFM captures much better the structure of the free-surface boundary layer. On the other hand, DASM is superior in obtaining the statistics

associated with free-surface signatures. The only shortcoming of these eddy-viscosity models is found in the prediction of the mean flow profile. This is overcome by the addition of a scale-similarity SGS model.

This research was financially supported by the Office of Naval Research under the program management of Dr E. P. Rood. Most of the computations were performed at the Aeronautical System Center on an IBM-SP3 as part of a DoD Challenge Project under the DoD HPC Modernization Program.

REFERENCES

Antonia, R. A. 1981 Conditional sampling in turbulence measurement. *Ann. Rev. Fluid. Mech.* **13**, 131–156.

Bardina, J., Ferziger, J. H. & Reynolds, W. C. 1983 Improved turbulence models based on large eddy simulation of homogeneous, incompressible turbulent flows. *Mech. Engng Dept., Stanford Univ. Rep.* TF-19.

Blackwelder, R. F. & Kaplan, R. E. 1976 On the wall structure of the turbulent boundary layer. *J. Fluid Mech.* **76**, 89–112.

Borue, V., Orszag, S. A. & Staroselsky, I. 1995 Interaction of surface waves with turbulence: direct numerical simulations of turbulent open-channel flow. *J. Fluid Mech.* **286**, 1–23.

Clark, R. A., Ferziger, J. H. & Reynolds, W. C. 1979 Evaluation of subgrid-scale models using an accurately simulated turbulent flow. *J. Fluid Mech.* **91**, 1–16.

Cortesi, A. B., Smith, B. L., Yadigaroglu, G. & Banerjee, S. 1999 Numerical investigation of the entrainment and mixing processes in neutral and stably-stratified mixing layers. *Phys. Fluids* **11**, 162–184.

David, E. 1993 Modélisation des écoulements compressibles et hypersoniques: une approche instationnaire. PhD thesis, Natl Polytech. Inst., Grenoble.

Dimas, A. A. & Fialkowski, L. T. 2000 Large-wave simulation (LWS) of free-surface flows developing weak spilling breaking waves. *J. Comput. Phys.* **159**, 172–196.

Domaradzki, J. A., Liu, W., Hartel, C. & Kleiser, L. 1994 Energy transfer in numerically simulated wall-bounded turbulent flows. *Phys. Fluids* **6**, 1583–1599.

Domaradzki, J. A. & Rogallo, R. S. 1990 Local energy transfer and nonlocal interactions in homogeneous, isotropic turbulence. *Phys. Fluids* A **2**, 413–426.

Dommermuth, D. G. & Novikov, E. A. 1993 Direct-numerical and large-eddy simulations of turbulent free-surface flows. *Sixth Intl Conf. on Numerical Ship Hydrodynamics, Iowa City.*

Germano, M. 1986 A proposal for a redefinition of the turbulence stresses in the filtered Navier–Stokes equations. *Phys. Fluids* **29**, 2323–2324.

Germano, M., Piomelli, U., Moin, P. & Cabot, W. H. 1991 A dynamic subgrid-scale eddy viscosity model. *Phys. Fluids* A **3**, 1760–1765.

Ghosal, S., Lund, T. S., Moin, P. & Akselvoll, K. 1995 A dynamic localization model for large-eddy simulation of turbulent flows. *J. Fluid Mech.* **286**, 229–255.

Handler, R. A., Swean, T. F. Jr., Leighton, R. I. & Swearingen, J. D. 1993 Length scales and the energy balance for turbulence near a free surface. *AIAA J.* **31**, 1998–2007.

Hartel, C., Kleiser, L., Unger, F. & Friedrich, R. 1994 Subgrid-scale energy transfer in the near-wall region of turbulent flows. *Phys. Fluids* **6**, 3130–3143.

Hodges, B. R. & Street, R. L. 1999 On simulation of turbulent nonlinear free-surface flows. *J. Comput. Phys.* **151**, 425–457.

Kim, J. 1983 On the structure of wall-bounded turbulent flows, *Phys. Fluids* **26**, 2088–2097.

Komori, S., Nagaosa, N., Murakami, Y., Chiba, S., Ishii, K. & Kuwahara, K. 1993 Direct numerical simulation of three-dimensional open-channel flow with zero-shear gas–liquid interface. *Phys. Fluids* A **5**, 115–125.

Kwak, D., Reynolds, W. C. & Ferziger, J. H. 1975 Three dimensional time dependent computation of turbulent flows. *Mech. Engng Dept., Stanford Univ. Rep.* TF-5.

Lam, K. & Banerjee, S. 1988 Investigation of turbulent flow bounded by a wall and a free surface. In *Fundamentals of Gas-Liquid Flows* (ed. E. Michaelides & M. P. Sharma), pp. 29–38. ASME.

Leonard, A. 1974 Energy cascade in large-eddy simulation of turbulence fluid flows. 237–248.

Lesieur, M. & Métais, O. 1996 New trends in large-eddy simulations of turbulence. *Ann. Rev. Fluid. Mech.* **28**, 45–82.

Lilly, D. K. 1992 A proposed modification of the Germano subgrid-scale closure method. *Phys. Fluids* A **4**, 633–635.

Liu, S., Meneveau, C. & Katz, J. 1994 On the properties of similarity subgrid-scale models as deduced from measurements in a turbulence jet. *J. Fluid Mech.* **275**, 83–119.

Lombardi, P., De Angelis, V. & Banerjee, S. 1996 Direct numerical simulation of near-interface turbulence in coupled gas-liquid flow. *Phys. Fluids* **8**, 1643–1665.

Mangiavacchi, N., Gundlapalli, R. & Akhavan, R. 1994 Dynamics of a turbulent jet interacting with a free surface. In *Free-Surface Turbulence* (ed. E. P. Rood & J. Katz), pp. 69–83. ASME.

Mattingly, G. E. & Criminale, W. O. 1972 The stability of an incompressible two-dimensional wake. *J. Fluid Mech.* **51**, 233–272.

McMillan, O. J., Ferziger, J. H. & Rogallo, R. S. 1980 Tests of new subgrid-scale models in strained turbulence. *AIAA Paper* 80-1339.

Meneveau, C. & Katz, J. 2000 Scale-invariance and turbulence models for large-eddy simulation. *Ann. Rev. Fluid. Mech.* **32**, 1–32.

Moin, P., Squires, K., Cabot, W. & Lee, S. 1991 A dynamic subgrid-scale model for compressible turbulence and scalar transport. *Phys. Fluids* A **3**, 2746–2757.

Pan, Y. & Banerjee, S. 1995 A numerical study of free-surface turbulence in channel flow. *Phys. Fluids* **7**, 1649–1664.

Perot, B. & Moin, P. 1995 Shear-free turbulent boundary layers. Part 1. Physical insights into near-wall turbulence. *J. Fluid Mech.* **295**, 199–227.

Piomelli, U., Cabot, W. H., Moin, P. & Lee, S. 1991 Subgrid-scale backscatter in turbulent and transitional flows. *Phys. Fluids* A **3**, 1766–1771.

Piomelli, U., Yu, Y. & Adrian R. J. 1996 Subgrid-scale energy transfer and near-wall turbulence structure. *Phys. Fluids* **8**, 215–224.

Rogallo, R. S. & Moin, P. 1984 Numerical simulation of turbulent flows. *Ann. Rev. Fluid. Mech.* **16**, 99–137.

Salvetti, M. V. & Banerjee, S. 1995 *A priori* tests of a new dynamic subgrid-scale model for finite-difference large-eddy simulations. *Phys. Fluids* **7**, 2831–2847.

Salvetti, M. V., Zang, Y., Street, R. L. & Banerjee, S. 1997 Large-eddy simulation of free-surface decaying turbulence with dynamic subgrid-scale models. *Phys. Fluids* **9**, 2405–2419.

Shen, L., Triantafyllou, G. S. & Yue, D. K. P. 2000 Turbulent diffusion near a free surface. *J. Fluid Mech.* **407**, 145–166.

Shen, L., Zhang, X., Yue, D. K. P. & Triantafyllou, G. S. 1999 The surface layer for free-surface turbulent flows. *J. Fluid Mech.* **386**, 167–212.

Smagorinsky, J. 1963 General circulation experiments with the primitive equations. Part I: The basic experiment. *Mon. Weather Rev.* **91**, 99–164.

Speziale, C. 1985 Galilean invariance of subgrid-scale stress models in the large-eddy simulation of turbulence. *J. Fluid Mech.* **156**, 55–62.

Walker, D. T., Leighton, R. I. & Garza-Rios, L. O. 1996 Shear-free turbulence near a flat free surface. *J. Fluid Mech.* **320**, 19–51.

Yoshizawa, A. 1986 Statistical theory for compressible turbulent shear flows, with the application to subgrid modelling. *Phys. Fluids* **29**, 2152–2164.

Zang, Y., Street, R. L. & Koseff, I. R. 1993 A dynamic mixed subgrid-scale model and its application to turbulence recirculation flows. *Phys. Fluids* A **5**, 3186–3196.